

# JWST MIRI color classification of mid-infrared selected galaxies

## MIRI color classification toward cosmic noon

E. Kilerci<sup>1,\*</sup>, T. Goto<sup>2</sup>, M. A. Malkan<sup>3</sup>, S. J. Kim<sup>2</sup>, C.-T. Ling<sup>4,5</sup>, C. K.-W. Wu<sup>2</sup>, T. Hashimoto<sup>6</sup>, S. C.-C. Ho<sup>7</sup>, Amos Y.-A. Chen<sup>2</sup>, and E. Göğüş<sup>8</sup>

<sup>1</sup> Department of Astronomy and Space Sciences, Science Faculty, İstanbul University, Beyazıt 34119, İstanbul, Türkiye  
e-mail: ecekilerci@istanbul.edu.tr

<sup>2</sup> Institute of Astronomy, National Tsing Hua University, 101, Section 2. Kuang-Fu Road, Hsinchu, 30013, Taiwan (R.O.C.)

<sup>3</sup> Department of Physics and Astronomy, University of California Los Angeles, 430 Portola Plaza, Los Angeles, CA 90095, USA

<sup>4</sup> Department of Astronomical Science, SOKENDAI (The Graduate University for Advanced Studies), 2-21-1 Osawa, Mitaka, Tokyo, 181-8588, Japan

<sup>5</sup> National Astronomical Observatory of Japan, 2-21-1 Osawa, Mitaka, Tokyo 181-8588, Japan

<sup>6</sup> Department of Physics, National Chung Hsing University, No. 145, Xingda Rd., South Dist., Taichung, 40227, Taiwan (R.O.C.)

<sup>7</sup> Research School of Astronomy and Astrophysics, The Australian National University, Canberra, ACT 2611, Australia

<sup>8</sup> Sabancı University, Faculty of Engineering and Natural Sciences, 34956, İstanbul, Türkiye

Received XXX; accepted YYY

### ABSTRACT

**Context.** We investigated the *James Webb* Space Telescope photometric color classification of mid-infrared (MIR) selected galaxies at high redshifts, toward cosmic noon.

**Aims.** The aim of the present work is to obtain a  $z$ -dependent mid-infrared (MIR) photometric galaxy classification tool based on broad spectral emission and absorption lines using the JWST Mid-Infrared Instrument (MIRI) and its broadband filters.

**Methods.** We used the largest *Spitzer* MIR spectral database to obtain synthetic photometry in the JWST/MIRI filters. We formed MIRI filter combinations to trace the strong polycyclic aromatic hydrocarbon (PAH) emission features and the  $9.7\ \mu\text{m}$  silicate feature in seven redshift windows from  $z = 0.25 - 2.10$ .

**Results.** We present  $z$ -dependent MIRI color–color plots that separate active galactic nuclei (AGN), star-forming galaxies (SFGs), and silicate absorption-dominated galaxies up to  $z \sim 2$ . We applied the photometric MIR colors to the largest ( $\sim 34\ \text{arcmin}^2$ ) MIRI survey called the Systematic Mid-infrared Instrument Legacy Extragalactic Survey (SMILES), to identify AGN, SFGs, and Si-absorption dominated galaxies out to substantial redshifts. Our JWST/MIRI SFGs sample includes galaxies with total IR luminosities of  $10^{9.2} \sim 10^{11.9}\ L_{\odot}$  at  $0.9 \leq z < 1.57$ . The majority of them are consistent with the  $z \sim 1$  main sequence. We also identified the first examples of  $z \sim 1$  galaxies with deep silicate absorption.

**Key words.** infrared: galaxies – galaxies: high-redshift – galaxies: active – galaxies: star formation – galaxies: general

## 1. Introduction

The mid-infrared (MIR) spectra of galaxies are essential probes into the nature of different populations, such as active galactic nuclei (AGN) and star-forming galaxies (SFGs), even when their optical emission is largely obscured by dust. Distinguishing galaxy populations at higher- $z$ , toward cosmic noon, is important for tracking the evolution of cosmic star formation ((CSFH) e.g., Magnelli et al. 2013) and the black hole accretion history ((BHAH) e.g., Yang et al. 2023a) across cosmic time. The strongest spectral features in the MIR wavelengths are the polycyclic aromatic hydrocarbon (PAH) emission features at  $3.3\ \mu\text{m}$ ,  $6.2\ \mu\text{m}$ ,  $7.7\ \mu\text{m}$ ,  $11.2\ \mu\text{m}$ ,  $12.7\ \mu\text{m}$ , (hereafter PAH33, PAH62,

PAH77, PAH112, PAH127) and the silicate (Si) emission and absorption features at  $9.7\ \mu\text{m}$  (hereafter Si97) and  $18\ \mu\text{m}$ . While the PAH emission lines are tracers of star formation activity (see, e.g., Peeters et al. 2004; Farrah et al. 2007; Calzetti et al. 2007), the silicate absorption features are generated by a bright continuum from AGN or starbursts, passing through a large amount of silicate dust producing Si–O stretching mode absorption. Therefore, deep silicate absorption features are uniquely capable of revealing the most heavily obscured AGN (see, e.g., Spoon et al. 2001, 2006; Levenson et al. 2007) or compact starbursts (see, e.g., Armus et al. 2004; Spoon et al. 2007).

In the pre-JWST era, the Infrared Space Observatory (*ISO*, Kessler et al. 1996) and *Spitzer* space telescope’s (Werner et al. 2004) Infrared Spectrograph (IRS, Houck et al. 2004) provided

\* Corresponding author

MIR spectra of mostly low-redshift galaxies. Spoon et al. (2007) examined the IRS and *ISO* spectra of AGN, starburst galaxies, infrared galaxies (IRGs), luminous infrared galaxies (LIRGs), and ultraluminous infrared galaxies (ULIRGs), and divided them into nine groups (ranging between continuum-, AGN-, PAH-, or absorption- dominated MIR spectra) according to the equivalent width (EQW) of the  $6.2\ \mu\text{m}$  emission line and the strength of the  $9.7\ \mu\text{m}$  silicate feature ( $S_{\text{sil}}$ , the negative of the apparent Si optical depth defined as Spoon et al. 2007, Eq. (1)). An extended study of more than 3000 *Spitzer* IRS spectra (Spoon et al. 2022) show that by using the PAH62 emission line EQW (hereafter PAH62 EQW) and the  $S_{\text{sil}}$  galaxies can be sorted into three main MIR spectral classes: (1) star-forming galaxies with strong PAH emission and weak silicate features (referred as ‘1C’ galaxies in Spoon et al. 2022); (2) strongly AGN-dominated galaxies with no or little PAH emission and weak silicate emission or absorption (referred as ‘1A’ galaxies in Spoon et al. 2022); (3) Si absorption-dominated galaxies with weak or undetectable PAH emission, whose power source can be an ultracompact nuclear starburst or AGN (referred as ‘3A’ galaxies in Spoon et al. 2022). To cover the large range of MIR spectra of galaxies, five additional intermediate spectral classes are introduced in the diagnostic diagram of Spoon et al. (2022) (their Fig. 14): (i) AGN with moderate PAH features as in normal star-forming galaxies (referred as ‘1B’ galaxies in Spoon et al. 2022); (ii) dusty star-forming galaxies with moderate PAH features and  $S_{\text{sil}}$  (referred as ‘2B’ galaxies in Spoon et al. 2022); (iii) dusty star-forming galaxies with strong PAH features (referred as ‘2C’ galaxies in Spoon et al. 2022); (iv) dusty AGN with moderate  $S_{\text{sil}}$  (referred as ‘2A’ galaxies in Spoon et al. 2022); (v) Si absorption-dominated SFGs galaxies with PAH emission (referred as ‘3B’ galaxies in Spoon et al. 2022). Dusty systems such as ULIRGs (with IR luminosities ( $L_{\text{IR}}$ )  $10^{12}L_{\odot} < L_{\text{IR}} < 10^{13}L_{\odot}$ ) and LIRGs ( $10^{11}L_{\odot} < L_{\text{IR}} < 10^{12}L_{\odot}$ ) (e.g., Sanders et al. 1988; Veilleux et al. 2002) are mainly in classes 2A3B (e.g., Armus et al. 2004; Spoon et al. 2007). Based on the galaxy evolution scenarios of U/LIRGs (e.g., Hopkins et al. 2008b), the MIR spectral diagnostic diagram may be interpreted as an evolutionary sequence starting from 1C or 1B mergers and reaching the 1A pure AGN phase after the dust-covered phase of interacting galaxies in 2A–3B (Spoon et al. 2022).

Since large spectroscopic surveys in the MIR are not practical, the MIR photometric color selection of different galaxies, such as AGN, obscured AGN, compact obscured nuclei (CONs), star-forming galaxies (SFGs), and AGN+star-forming composites (e.g., Stern et al. 2012; Mateos et al. 2013; Kirkpatrick et al. 2013, 2017; Rovilos et al. 2014; Ichikawa et al. 2019; García-Bernete et al. 2022; Kirkpatrick et al. 2023), is a powerful method to select galaxies for spectroscopic follow-ups and perform statistical analysis of large samples. The Mid-Infrared Instrument (MIRI), Rieke et al. 2015; Wright et al. 2023) of JWST provides continuous photometric coverage with its narrow and broad bands in the range  $\sim 5\text{--}25\ \mu\text{m}$ , with a uniquely high sensitivity, down to  $1\ \mu\text{Jy}$  (e.g., Ling et al. 2022; Wu et al. 2023; Yang et al. 2023b; Kirkpatrick et al. 2023). This unprecedented sensitivity allows us, for the first time, to identify fainter galaxies with  $L_{\text{IR}} = 10^9 - 10^{10}L_{\odot}$  at  $z = 1 - 2$  (Kirkpatrick et al. 2023). MIRI performs imaging with nine filter bandpasses, F560W, F770W, F1000W, F1280W, F1500W, F1800W, F2100W, and F2550W, centered at 5.6-, 7.7-, 10.0-, 11.3-, 12.8-, 15.0-, 18.0-, 21.0-, and  $25.5\ \mu\text{m}$ ; respectively. Before the launch of JWST, Kirkpatrick et al. (2017) used IR SED templates of high-redshift dust-rich galaxies with strong PAH emission and presented a redshift-dependent MIRI color selection covering the  $z = 1 - 2$

range to identify AGN, SFGs, and composite mixtures of both. Their color selection traces the  $6.2$  and  $7.7\ \mu\text{m}$  PAH features and the  $35\ \mu\text{m}$  stellar minimum at  $z \sim 1$ ,  $z \sim 1.5$ , and  $z \sim 2$ . Kirkpatrick et al. (2023) present an updated color selection (which does not require redshift information) sensitive to PAH62 and PAH77 that separates AGN, SFGs, and MIR weak galaxies based on the MIRI survey obtained for The Cosmic Evolution Early Release Science (CEERS) program in the Extended Groth Strip (EGS). García-Bernete et al. (2022) presents MIRI color diagrams to select the most obscured galaxy nuclei in CONs based on SED model fitting results of local U/LIRGs selected from *Spitzer* IRS spectra sample of Spoon et al. (2022). Lin et al. (2024) introduced a color–color diagram to select particularly bright sources at  $15\ \mu\text{m}$  that are likely PAH luminous galaxies at  $z \sim 1$  in the CEERS MIRI survey. MIR selection methods have long been used to identify AGN (e.g., Stern et al. 2012; Assef et al. 2013). More recently, Bornancini & García Lambas (2020) analyzed the host galaxy properties of obscured and unobscured AGN selected in the MIR, providing complementary insights into the nature of these populations. These studies provide a broader context for our approach, which extends MIR diagnostics into the JWST/MIRI regime with redshift-dependent color cuts.

With the new sensitivity and continuous photometric coverage of MIRI, the MIR spectral features of galaxies can be traced out to cosmic noon ( $z \sim 1 - 2.0$ ) (e.g., Yang et al. 2023b; Kirkpatrick et al. 2023). The aim of this study is to develop and apply a  $z$ -dependent color–color diagnostic for the three main MIR spectral classes defined by PAH62 EQW and  $S_{\text{sil}}$  (Spoon et al. 2022). We focus on identifying SFGs, AGN-dominated, and Si absorption-dominated galaxies by tracing PAH62, PAH77, PAH112, PAH127, and Si  $9.7\ \mu\text{m}$  through MIRI bands over the  $0.25 \leq z \leq 2.10$  range, where the available *Spitzer* IR spectra are very sparse (e.g., there are just a few *Spitzer* spectra for Si absorption-dominated galaxies in the 3A and 3B classes at  $z \geq 1$ ). We used the largest *Spitzer* spectral database, The Infrared Database of Extragalactic Observables (IDEOS sample; Hernán-Caballero et al. 2016; Spoon et al. 2022) for our investigation.

The structure of this paper is as follows. We present the IDEOS sample in §2.1. In §2.2 we introduce our color selection criteria for SFGs, AGN-dominated galaxies, and Si absorption-dominated galaxies at different  $z$  values. We present the SMILES JWST/MIRI photometric survey, to which we apply our color diagnostics, in Sect. 3. In §4 we describe the MIRI galaxy classification in the SMILES sample. The main results and discussion of our analysis are presented in §6. Our main conclusions are summarized in §7. In this work we adopt a flat  $\Lambda$  cold dark matter cosmology with  $H_0 = 72\ \text{km s}^{-1}\ \text{Mpc}^{-1}$ ,  $\Omega_{\Lambda} = 0.7$ , and  $\Omega_{\text{m}} = 0.3$  (Spergel et al. 2003).

## 2. Sample and analysis

### 2.1. *Spitzer* IDEOS sample

The IDEOS database (Hernán-Caballero et al. 2016; Spoon et al. 2022) provides homogeneously analyzed archival *Spitzer* IRS spectra of 3335 galaxies with  $S_{\text{sil}}$ , PAH line fluxes and equivalent widths, rest-frame continuum flux densities, synthetic MIRI photometry measurements, and MIR classification. To investigate redshift-dependent MIRI colors of different types of MIR galaxies we used *Spitzer* IRS spectra from the IDEOS sample. To represent galaxies in different MIR classes we selected spectra with signal-to-noise ratio (S/N)  $\geq 5$  at least in two continuum regions at rest frame  $6.6\ \mu\text{m}$  and  $9\ \mu\text{m}$  or  $6.6\ \mu\text{m}$  and  $13.25\ \mu\text{m}$

or  $9\ \mu\text{m}$  and  $11.25\ \mu\text{m}$ . This selection yielded large numbers of spectra in each MIR class: 805 1A, 307 1B, 494 1C, 50 2A, 134 2B, 72 2C, 19 3A, and 31 3B. In total, our IDEOS sample included 1912 spectra. We convolved these spectra with MIRI filters following the synthetic photometric flux density recipe given by Spoon et al. (2022), namely, we measured the photon-weighted mean flux density over the bandpass of the filter as given by their equation 7.

## 2.2. Color analysis

As noted by Spoon et al. (2022), their MIR spectral classification is successful in distinguishing three main classes: pure SFGs (1C), AGN-dominated galaxies (1A), and Si absorption-dominated galaxies (3A). Since we rely on their MIR classification, here we search for colors to separate especially the pure SFGs, AGN-dominated galaxies, and Si absorption-dominated galaxies between  $0.1 \leq z \leq 2$ . First, we expanded the MIR spectral classification based on PAH62 to other PAH lines since the PAH62 EQW of our IDEOS sample strongly correlates with PAH77 EQW, PAH112 EQW, PAH127 EQW as shown in Appendix A. We examined various color-color combinations to trace PAH emission features, Si absorption feature, and hot-dust-dominated continuum. We determined the  $z$  ranges at which the Si and PAH features can be probed in MIRI bands. The  $9.7\ \mu\text{m}$  Si absorption feature shifts to  $9.7(1+z)$ ; at  $z = 0.25\text{--}0.30$ ,  $0.58\text{--}0.65$ ,  $0.9\text{--}0.92$ ,  $1.0\text{--}1.1$ , and  $1.5\text{--}1.6$  it enters the  $12.8\ \mu\text{m}$ ,  $15.0\ \mu\text{m}$ ,  $18.0\ \mu\text{m}$ ,  $21.0\ \mu\text{m}$  and  $25.5\ \mu\text{m}$  imaging bands, respectively. Therefore, it can be traced by MIRI up to  $z \sim 1.6$ . The examined MIRI color-color diagrams combining Si97 and PAH62, PAH77, PAH112, PAH127 colors at different redshift intervals are shown in Fig. 1.

### 2.2.1. Classification of each MIR class

First, we used the Gaussian mixture modeling (GMM, Maas et al. 2015, e.g.,) to determine the regions where different MIR classes can be distinguished from each other. GMM is a clustering algorithm to model overlapping and not well-separated clusters by assuming that the data are created from a mixture of Gaussian distributions. We used the Python package SKLEARN.MIXTURE from SCIKIT-LEARN (Pedregosa et al. 2011). We applied GMM to each MIR class by allowing one, two, or three separate Gaussian distributions, each with its mean, covariance, and weight parameters. Since our color-color diagrams are in a 2D space, the mean is a 2D vector and the covariance is a  $2 \times 2$  matrix. The ellipses in the panels of Fig. 1 show the obtained model regions for each MIR class; model regions are tabulated in Table B.1 in Appendix B.

In all panels in Fig. 1, a distinct color region of class 3A can be seen in the lower left corner, which does not overlap with other class regions. This is caused by the large flux difference between Si97 and PAH62, and PAH77 that is expected to be large for absorption-dominated galaxies. For example, at  $z = 0.25\text{--}0.30$ , PAH62 is at F770W, PAH77 is at F1000W, Si97 is at F1280W. Therefore, the  $F(12\ \mu\text{m})/F(7\ \mu\text{m})$  and  $F(12\ \mu\text{m})/F(10\ \mu\text{m})$  measure the flux difference between Si97 and PAH62, and PAH77, respectively. At  $z = 0.58\text{--}0.65$  range, PAH62 is at F1000W, PAH77 is at F1280W, PAH113 is at F1800W, PAH127 is at F2100W, and Si97 is at F1500W. And at  $z = 0.9\text{--}0.92$  range, PAH77 is at F1500W, PAH127 is at F2550W, Si97 is at F1800W. Similarly, at  $z = 1.0\text{--}1.1$  range, PAH62 is at F1280W, PAH77 is at F1500W, Si97 is at F2100W.

And at  $z = 1.5\text{--}1.6$  range, PAH62 is at F1500W, PAH77 is at F2100W, Si97 is at F2550W. As shown in each panel in Fig. 1, for each  $z$  range examined here, similar regions are detected for galaxies 3A and 3A-3B classes due to the large flux difference between Si97 and PAH lines. In most panels, 2A galaxies with relatively smaller flux difference between Si97 and PAH lines locate above the absorption-dominated galaxies.

AGN produce a strong continuum from hot dust, but no PAH emission. For example, at  $z = 0.25\text{--}0.30$  continuum regions  $6\text{--}6.9\ \mu\text{m}$ ,  $7\text{--}8.3\ \mu\text{m}$ , and  $9.5\text{--}11.1\ \mu\text{m}$  are at F770W, F1000W, and F1280W, respectively. For (unabsorbed) AGN, the  $F(12\ \mu\text{m})/F(7\ \mu\text{m})$  and  $F(12\ \mu\text{m})/F(10\ \mu\text{m})$  represent the relatively small flux difference between the two continua. Therefore, 1A and 1A-1B AGN are located at similar regions at the top in each panel due to the small flux difference in the colors on the y-axis.

Here we find that at different  $z$  ranges, the MIR class region boundaries are similar when obtained from the ratios of MIRI bands where Si and the same PAH lines shift. We note that our attempt to define distinct regions for each MIR class, is mostly successful for the 1A, 3A, and 3A-3B classes. However, for other classes the defined regions heavily overlap with each other.

### 2.2.2. Classification of AGN, SFGs, and composite galaxies

In addition to the defined distinct regions designated to select only a single MIR class in the GMM analysis, we combine 1A-1B-2A as AGN, 1C-2C as SFGs to separate AGN and SFGs. Modeled AGN (orange), SFGs (green) region ellipses are shown in Fig. 2. The modeled regions are listed in Table B.2 in Appendix B.

## 2.3. Comparison with MIRI color classifications in the literature

Kirkpatrick et al. (2017) and Kirkpatrick et al. (2023) present redshift-dependent MIRI color selection for AGN, SF and composite galaxies. Unlike our study, their galaxy classification is based on SED templates, and galaxies are classified according to their AGN MIR contribution in the  $5\text{--}15\ \mu\text{m}$  wavelength range ( $f_{\text{AGN}}^{5-15\ \mu\text{m}}$ ). They define AGN as  $f_{\text{AGN}}^{5-15\ \mu\text{m}} \geq 0.7$ , SFGs as  $f_{\text{AGN}}^{5-15\ \mu\text{m}} < 0.3$  and composites as  $0.3 \leq f_{\text{AGN}}^{5-15\ \mu\text{m}} < 0.7$ . In Fig. 3 we show the color-color diagrams adopted from Kirkpatrick et al. (2017) (left and middle panels). The inner solid cyan circle shows the AGN circle defined by Kirkpatrick et al. (2017). Most of the 1A AGN in our sample are located in this region, but there are also composite AGN+SFGs. Between the inner and outer circles and outside the outer circle, we have all types of galaxies, AGN, SF, and composites. As noted by Kirkpatrick et al. (2023) the color selection in these two diagrams is not good enough to select AGN in MIRI surveys such as CEERS. Therefore, they introduced an updated color-color diagram, shown in the right panel of Fig. 3. Here they define the AGN region with the cyan hexagon. Our sample has 1A-1B-2A AGN, 3A, and 2B galaxies inside their hexagon. In these diagrams, AGN and SFGs regions obtained by GMM analysis are shown by orange and dark green ellipses. These regions are listed in Table B.3 in Appendix B.

The AGN and SFGs limits of Kirkpatrick et al. (2017) and Kirkpatrick et al. (2023) are inside the AGN and SFGs regions obtained by the GMM analysis; therefore, our regions are compatible with their limits. Compared to these studies, we determined regions in these color diagrams where galaxies of different MIR spectral types can be more accurately distinguished.

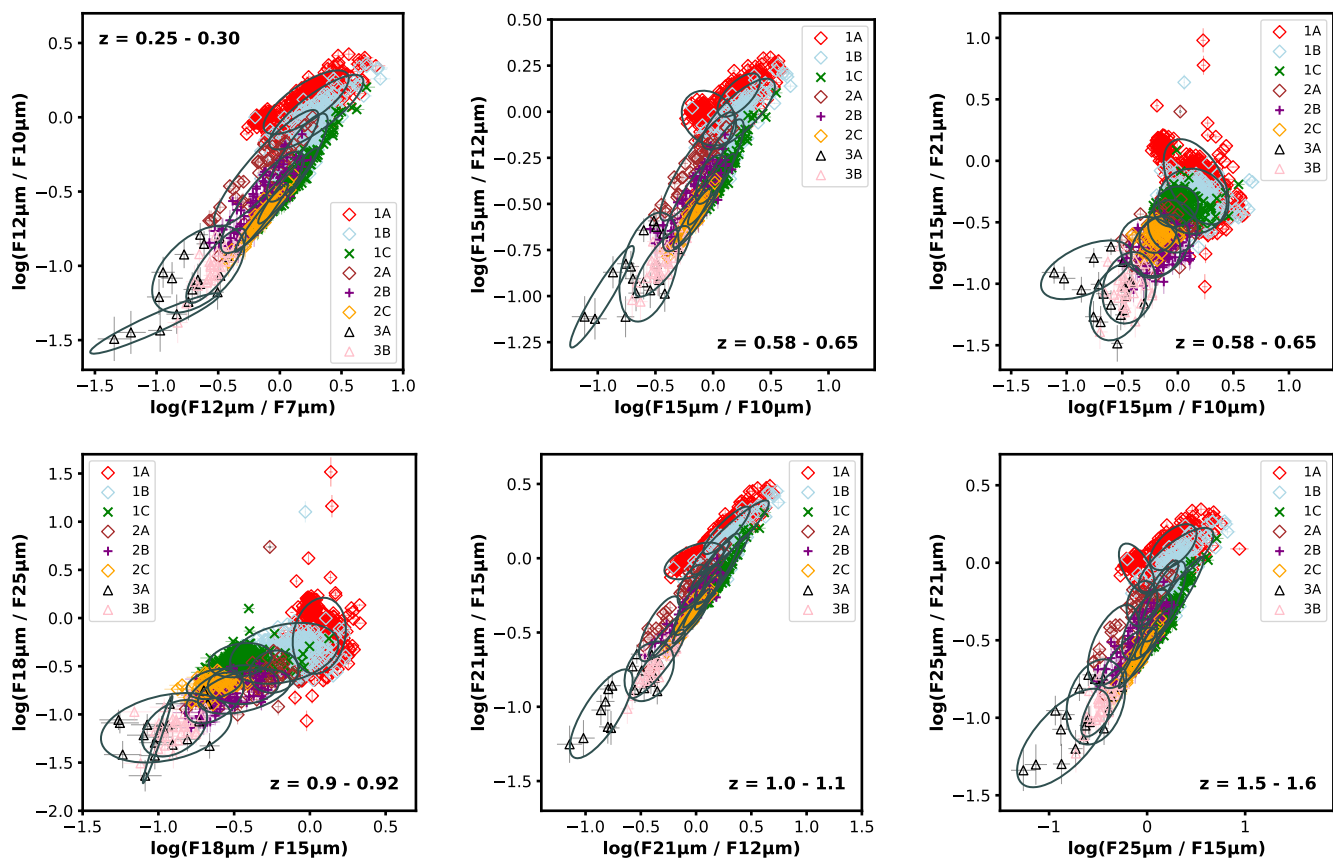


Fig. 1: MIRI colors of different MIR class IDEOS galaxies at  $z = 0.25\text{--}0.30$  (top left panel),  $z = 0.58\text{--}0.65$  (top right and middle left panels),  $z = 0.90\text{--}0.92$  (middle right panel),  $z = 1.00\text{--}1.10$  (bottom left panel),  $z = 1.50\text{--}1.60$  (bottom right panel). The MIR class symbol code is given in the legend. In each panel, the ellipses represent a 2D Gaussian component for the MIR class subregions.

### 3. MIR spectral classification of MIR detected galaxies in SMILES

#### 3.1. SMILES survey

The Systematic Mid-infrared Instrument Legacy Extragalactic Survey (SMILES; Alberts et al. 2024; Rieke et al. 2024) is a MIRI imaging survey of 34 arcmin<sup>2</sup> in the Great Observatories Origins Deep Survey South (GOODS-S) Hubble Ultra Deep Field (HUDF; Beckwith et al. 2006) field. It includes the  $F560W$ ,  $F770W$ ,  $F1000W$ ,  $F1280W$ ,  $F1500W$ ,  $F1800W$ ,  $F2100W$ ,  $F2550W$  MIRI broad bands. SMILES is the largest, deepest MIRI survey with superb spatial resolution (between 0.19 to 0.86 arcsec) ever completed. Therefore, it provides an ideal data set for our study.

SMILES survey area also includes ancillary data, including ultradeep NIRCcam imaging from the JWST Advanced Deep Extragalactic Survey (JADES; Eisenstein et al. 2023; Rieke et al. 2023), JWST Extragalactic Medium-band Survey (JEMS; Williams et al. 2023; Rieke et al. 2023), Hubble Space Telescope (HST) imaging from multiple surveys (e.g., Grogin et al. 2011), NIRCcam grism spectroscopy from the First Reionization Epoch Spectroscopically Complete Observations (FRESCO; Oesch et al. 2023).

#### 3.2. SMILES data

We used the SMILES Data Release 1 (DR1) clean catalog (Alberts et al. 2024) with 3096 sources detected at  $\geq 4\sigma$  in either the  $F560W$  or  $F770W$  bands. We refer to Alberts et al. (2024) for the details of the photometric measurements. The catalog provides aperture-corrected photometry in five circular apertures and in a 2.5 $\times$ -scaled Kron aperture. In this work, we used 2.5 $\times$ -scaled Kron aperture measurements as recommended by Rieke et al. (2023).

To apply our  $z$ -dependent color selection obtained in this work we required  $z$  determinations from the ancillary data and the literature. We matched the SMILES DR1 catalog with JADES Data Release 3 (DR3) catalog<sup>1</sup> (D'Eugenio et al. 2024) within 0.3 arcsec separation, to obtain spectroscopic redshifts ( $z_s$ ) of 286 SMILES sources (from their  $z_{Spec}$  column). We matched SMILES DR1 catalog with MUSE Hubble Ultra Deep Field surveys DR 2 Main source catalog (Bacon et al. 2023) within 0.6 arcsec separation, to obtain  $z_s$  of 594 SMILES sources (from their  $z$  column). We matched SMILES DR1 catalog with CANDELS GOODS-S Redshift catalog (Kodra et al. 2023) within 0.6 arcsec to obtain  $z_s$  of 467 SMILES sources. In total, we obtained spectroscopic redshifts for unique 1101 sources (from their  $z_{spectroscopic}$  column). We matched the SMILES DR1 catalog with JADES NIRCcam photometric red-

<sup>1</sup> jades\_dr3\_medium\_gratings\_public\_gs\_v1.1.fits

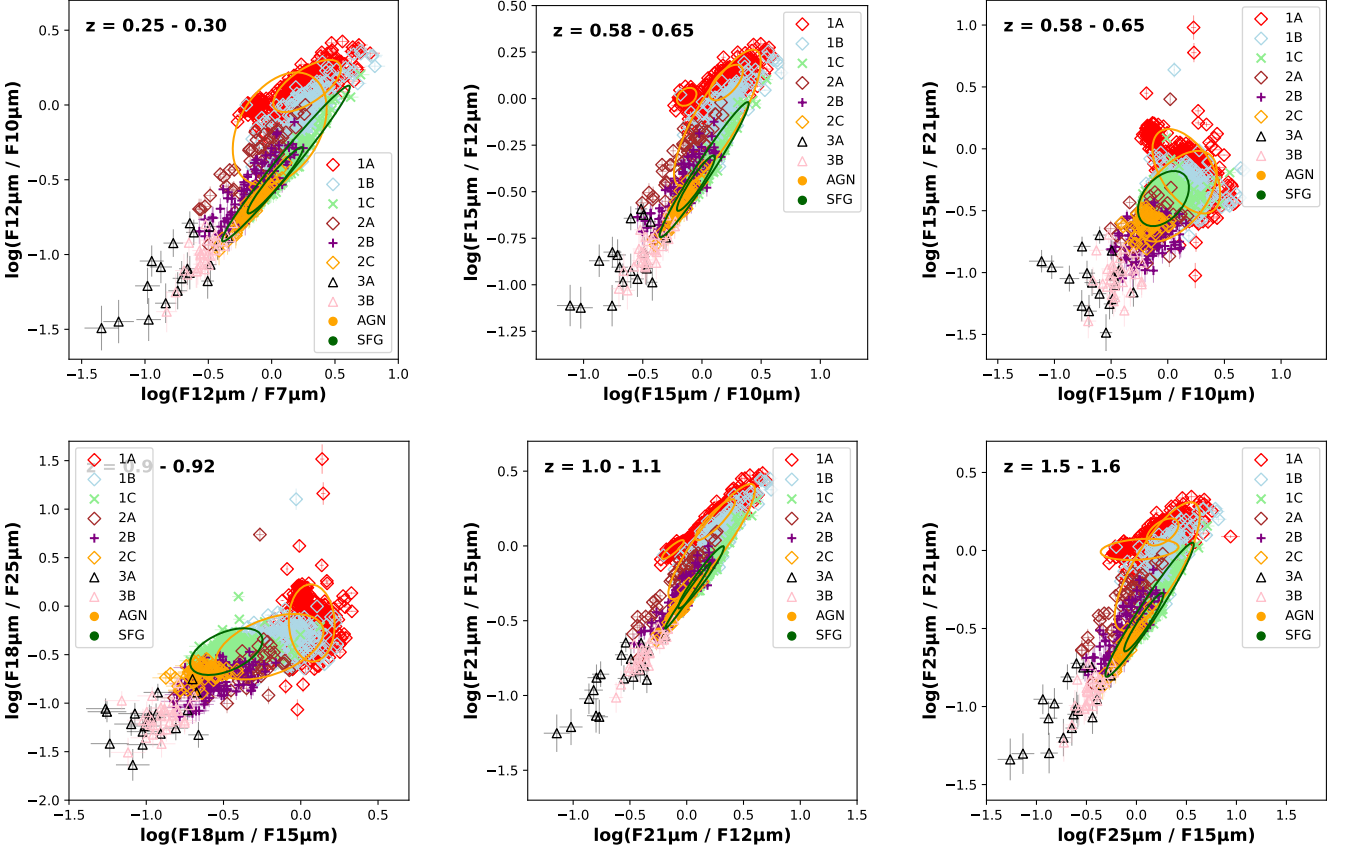


Fig. 2: Subregions obtained from the GMM analysis for AGN (1A-1B-2A combined) and SFGs (1C-2C combined). The regions of AGN and SFGs are shown as orange and green ellipses, respectively.

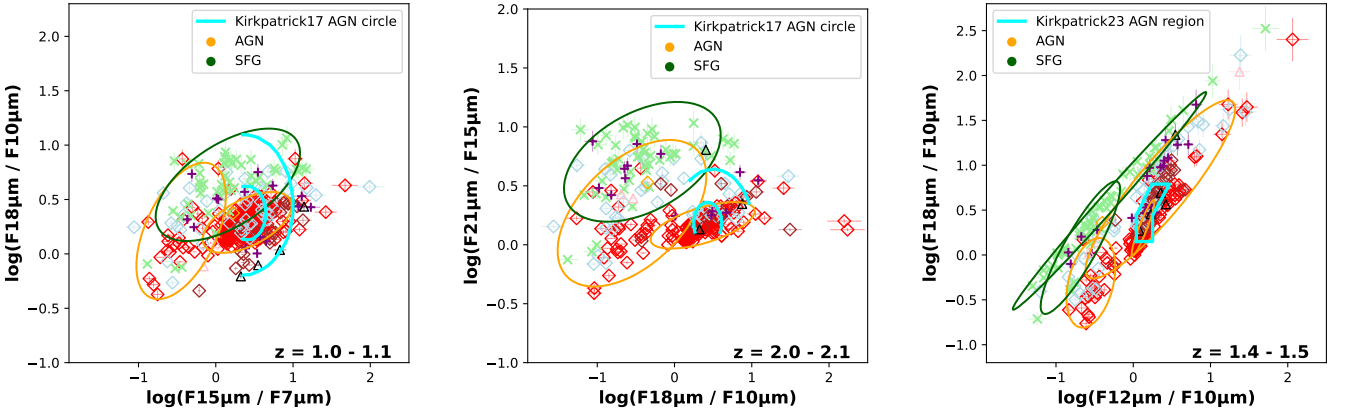


Fig. 3: Left and middle panels: Color-color diagrams adopted from Kirkpatrick et al. (2017). The solid cyan circles are their AGN, composite, and SFGs regions. Right panel: Color-color diagram Kirkpatrick et al. (2023). The cyan hexagon defines their AGN region. In all panels, the dark green and orange ellipses respectively represent the SFGs and AGN regions obtained by the GMM analysis.

shift catalog<sup>2</sup> (Rieke et al. 2023) within 0.3 arcsec and obtained the photometric redshifts ( $z_p$ ) of 2864 sources obtained by the template-fitting code EAZY (Brammer et al. 2008) to the JADES and JEMS JWST/NIRCam and HST/ACS photometry

(their *EAZY\_z\_a* column). Additionally, since we used SMILES AGN sample of Lyu et al. (2024) in §6.2 for 201 overlapping SMILES sources (within 0.6 arcsec positional match), we used their revised photometric/spectroscopic redshifts compared to CANDELS, JADES and JEMS catalogs.

<sup>2</sup> hlsj\_jades\_jwst\_nircam\_goods-s-deep\_photometry\_v2.0\_catalog.fits

#### 4. MIRI color classification of SMILES sample

We performed classification of SMILES sources by taking into account both the colors and the  $z$  of the sources (for  $z_p$  values we required  $z_p - 1\sigma$  and  $z_p + 1\sigma$  to be within the applied  $z$  range). We used GMM models (listed in Tables B.1, B.2, and B.3) trained on IDEOS MIR classes.

We used both Gaussian Mixture Model prediction and Mahalanobis distance minimization for initial classification. Gaussian Mixture Model prediction predicts the class of a source based on maximum likelihood assignment. Alternatively, Mahalanobis distance criterion assigns each object to the closest GMM component. While both approaches assign sources to the same dominant classes in most cases, discrepancies arise for outlier points close to decision boundaries. Mahalanobis distance emphasizes proximity to class centroids while incorporating shape and orientation of the class ellipses. GMM prediction, in contrast, may assign outliers to components with broader covariance structures. While both methods yield largely consistent classifications, the Mahalanobis approach tends to provide more conservative assignments, especially for sources lying at the intersection of multiple ellipses. Therefore, we calculated Mahalanobis distance between each data point and each GMM component for classification of SMILES sources. We used 95.4% confidence as a threshold to assign the MIR class based on highest confidence.

All of the  $z$ -dependent applied color limits are shown in Fig. 4. We identified 121 AGN (including 1A, 1B, 2A), 154 SFGs (including 1C, 2C), and six Si absorption-dominated galaxies (3A class), at various redshifts up to  $z \geq 2$ .

#### 5. SED analysis of the selected SFGs

To investigate the nature of the 154 MIRI-selected SFGs we combined the available photometric data and performed SED analysis with the Code for Investigating Galaxy Emission (CIGALE; Noll et al. 2009; Serra et al. 2011; Boquien et al. 2019; Yang et al. 2022) version 2022.1 (Yang et al. 2022). We used 31 filters in the SED fitting: nine HST filters (the HST/Advanced Camera for Surveys (ACS)  $F435W$ ,  $F606W$ ,  $F775W$ ,  $F814W$ ,  $F850LP$  and HST/WFC3  $F105W$ ,  $F125W$ ,  $F140W$ ,  $F160W$ ) from Rieke et al. (2023); 14 NIRC wide and medium filters ( $F090W$ ,  $F115W$ ,  $F150W$ ,  $F182M$ ,  $F200W$ ,  $F210M$ ,  $F277W$ ,  $F335M$ ,  $F356W$ ,  $F410M$ ,  $F430M$ ,  $F444W$ ,  $F460M$ , and  $F480M$ ) from Rieke et al. (2023); eight MIRI filters ( $F560W$ ,  $F770W$ ,  $F1000W$ ,  $F1280W$ ,  $F1500W$ ,  $F1800W$ ,  $F2100W$ , and  $F2550W$ ) from Alberts et al. (2024). We used Kron magnitudes as recommended by Rieke et al. (2023). We checked the flags indicating a star (FLAG\_ST), a nearby bright star (FLAG\_BS) and contaminating the photometry (FLAG\_BN) and used only the reliable photometry from the catalogs of Rieke et al. (2023). Additionally, when available, we used *Spitzer* MIPS photometry at  $70\mu\text{m}$  and *Herschel* PACS photometry at 100 and  $160\mu\text{m}$  for the 0.6 arcsec matched counterparts from the GOODS-*Herschel* catalog (Elbaz et al. 2011). However, only 29 SFGs and 15 AGN have reliable *Herschel* PACS photometry.

In addition, the FIR radiation, which is a strong indicator of SF in galaxies, has been detected (in the GOODS-*Herschel* catalog Elbaz et al. 2011) for 29 sources. Hence, at least 19 percent of the SFG candidates are secure SFGs.

CIGALE<sup>3</sup> is a SED analysis code designed especially for galaxies producing IR radiation (from near to far-IR). It combines the radiation produced by the stars, star formation, dust,

and AGN by balancing (e.g., Efstathiou & Rowan-Robinson 2003; da Cunha et al. 2008; Noll et al. 2009; Boquien et al. 2019) the ultraviolet/optical/near-IR radiation and the re-emitted mid- and far-IR radiation by dust. We used the CIGALE modules listed in Table 1 for different emission components contributing to the SED. Since all of the SFG candidates have  $z_s$  we fixed the source redshift in the SED analysis. To model the stellar component we used the delayed SFH optional exponential burst module (Boquien et al. 2019). We used the stellar population models synthesis models of Bruzual & Charlot (2003) and the Salpeter initial mass function (IMF) (Salpeter 1955) with solar metallicity. We adopted the `dustatt_modified_starburst` (Leitherer et al. 2002) that assumes the extinction law of Calzetti et al. (2000) for the dust attenuation. We allowed the color excess of nebular lines  $E(B - V)_{line}$  to vary between 0.05 and 4. We fixed the reduction factor for the stellar continuum attenuation as 0.44. We used the Draine et al. (2014) updated models for the dust emission and allowed a large range for the minimum radiation field ( $0.4 \leq U_{min} \leq 50$ ). We allowed the mass fraction of PAH to be between 1.77 and 7.32. We used the clumpy torus AGN model of (Stalevski et al. 2012, 2016) for the AGN component. We allowed all possible values of the average edge-on optical depth at  $9.7\mu\text{m}$ . We also allowed to have Type 1 and Type 2 AGN based on all available viewing angles. The fractional AGN emission contribution to the IR emission in the 8–1000  $\mu\text{m}$  range is shown by the  $frac_{AGN}$  parameter. To account for possible AGN strengths we allowed  $frac_{AGN}$  to be between 0 and 0.7. We show two examples of the best-fitting SEDs of the MIRI-selected SFGs at  $z \sim 1.5$  in Fig. 5.

CIGALE uses the given parameters and builds several model combinations (e.g., Boquien et al. 2019). The Bayesian method used in CIGALE measures the likelihood of each model compared to the dataset. CIGALE uses these likelihoods to give a probability distribution function of the parameters and provides the Bayesian uncertainties based on Bayesian analysis.

## 6. Results and discussion

### 6.1. MIRI color selection

The most important limitation of the color criteria proposed in this study is that they cannot select all galaxies belonging to a specific MIR spectral class. On the other hand, our color criteria have the advantage of selecting sources that can be distinguished from other classes. This purity is the most important difference from the color limit studies in the literature. Since our color limits are valid in small  $z$  intervals, we expect to have a low level of confusion between SFGs and AGN compared to previous studies (e.g., Kirkpatrick et al. 2023).

Since our color limits are based on the shift of the spectral lines through the MIRI bands, the proposed limits are redshift-dependent. Therefore, prior  $z$  knowledge is a second limitation of their application. Therefore, we suggest using these limits with secure  $z_s$  or  $z_p$  with low uncertainties.

Possible biases in selecting AGN, SFGs, and Si absorption-dominated galaxies by MIR colors include underrepresentation of each galaxy class, as they overlap in color space with other MIR classes. MIR color selection is sensitive to AGN-dominated emission, leading to biases, particularly mergers where extreme nuclear starbursts can mimic AGN signatures. While MIR color selection primarily identifies luminous, obscured AGN, it potentially overlooks starbursts that may also exhibit a similar signature. These selection biases can lead to misclassification that can

<sup>3</sup> <http://cigale.lam.fr/>

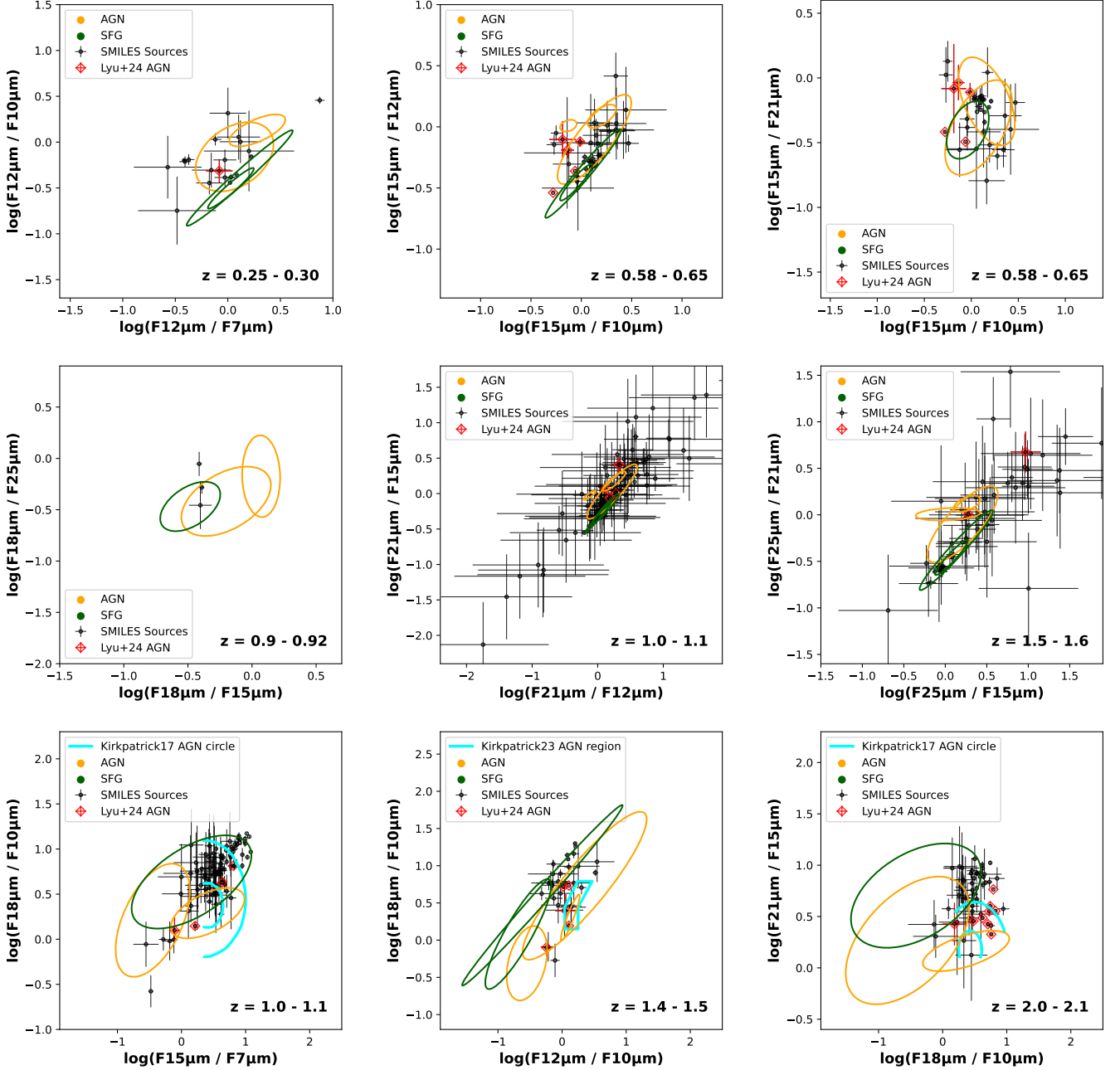


Fig. 4: MIRI colors of SMILES galaxies. The subregions obtained from the GMM analysis for AGN (1A-1B-2A combined), SFGs (1C-2C combined) are shown as the orange and dark green ellipses.

affect the completeness of AGN and SFGs identified by these diagnostics.

## 6.2. MIRI selected AGN toward cosmic noon

We performed SED analysis for the 121 MIRI-selected AGN candidates using the modules listed in Table 1 with a more comprehensive parameter setting for the AGN component ( $\tau_{\text{AGN}} = 3, 5, 7, 9, 11$ ;  $oa_{\text{AGN}} = 10, 20, 30, 40, 50, 60, 70, 80$ ;  $i = 0, 10, 20, 30, 40, 50, 60, 70, 80, 90$ ;  $frac_{\text{AGN}} = 0.0, 0.01, 0.05, 0.1, 0.2, 0.3, 0.4, 0.5, 0.6, 0.7, 0.8, 0.9$ ). We find that 31 of the 121 AGN candidates can be classified as AGN with  $frac_{\text{AGN}} \geq 0.2$  based on their SEDs. As a result of the SED analysis, we con-

sider 31 sources<sup>1</sup> as secure AGN selected by MIRI colors. For 36% AGN candidates, the SED selection agrees with the MIRI-color selection. Among the 79 candidates with  $frac_{\text{AGN}} < 0.2$ , 39 are dwarf galaxies with  $M_{\text{star}} < 10^{9.5} M_{\odot}$ . As shown in a recent MIRI SED analysis-based AGN classification study by Lyu et al. (2024), dwarf galaxies may appear to have MIR colors of AGN due to their reduced PAH and warmer dust emission. Therefore, 39 dwarf galaxies among 121 AGN candidates indicate a 32% contamination rate, potentially causing misclassifications.

<sup>1</sup> (SMILES IDs: 34, 38, 74, 90, 144, 153, 186, 327, 369, 373, 375, 436, 502, 529, 714, 796, 886, 1036, 1081, 1130, 1300, 1401, 1447, 1506, 1661, 1671, 1721, 1798, 1926, 2267, 2384)

Table 1: CIGALE modules

Parameters	Value
<i>Delayed SFH with optional exponential burst</i> (Boquien et al. 2019)	
e-folding time of the main stellar population [ $10^6$ yr]	500, 1000.0, 4000.0, 5000.0
Age of the galaxy's main stellar population [ $10^6$ yr]	500, 1000.0, 2000.0, 5000.0
e-folding time of the late starburst population [ $10^6$ yr]	50.0
Age of the late burst [ $10^6$ yr]	10.0
Mass fraction of the late burst population	0.00
multiplicative factor controlling the amplitude of SFR if normalization is True	1.0
<i>SSP</i> (Bruzual & Charlot 2003)	
Initial mass function	Salpeter (1955)
Metallicity	0.02
Age of separation between the young and old star populations	10.0
<i>Dust attenuation</i> (Charlot & Fall 2000)	
Logarithm of the V-band attenuation in the ISM	0.1, 0.17, 0.28, 0.46, 0.77, 1.29, 2.15, 3.59, 5.99, 10.0
Ratio of V-band attenuation from old and young stars	0.44
Power-law slope of the attenuation in the ISM	-0.7,-0.5
Power-law slope of the attenuation in the birth cloud	-0.7
<i>Dust emission</i> (Draine et al. 2014)	
Mass fraction of PAH ( $q_{PAH}$ )	1.12, 2.5, 3.9, 4.58, 5.95, 6.63, 7.32
Minimum radiation field ( $U_{min}$ )	0.1, 1.0, 10.0, 20.0, 50.0
Power-law slope $\alpha$ ( $\frac{dU}{dM} \propto U^\alpha$ )	2.0, 3.0
Fraction illuminated from $U_{min}$ to $U_{max}$	0.01, 0.1
<i>SKIRTOR AGN</i>	
$\tau_{AGN}$	3
$oa_{AGN}$	40, 70
$R_{AGN}$	20
inclination ( $i$ )	0, 10, 30, 80
$frac_{AGN}$ (computed for the 3-30 micron range)	0.0, 0.01, 0.03, 0.05, 0.1, 0.2, 0.3, 0.4, 0.5, 0.6

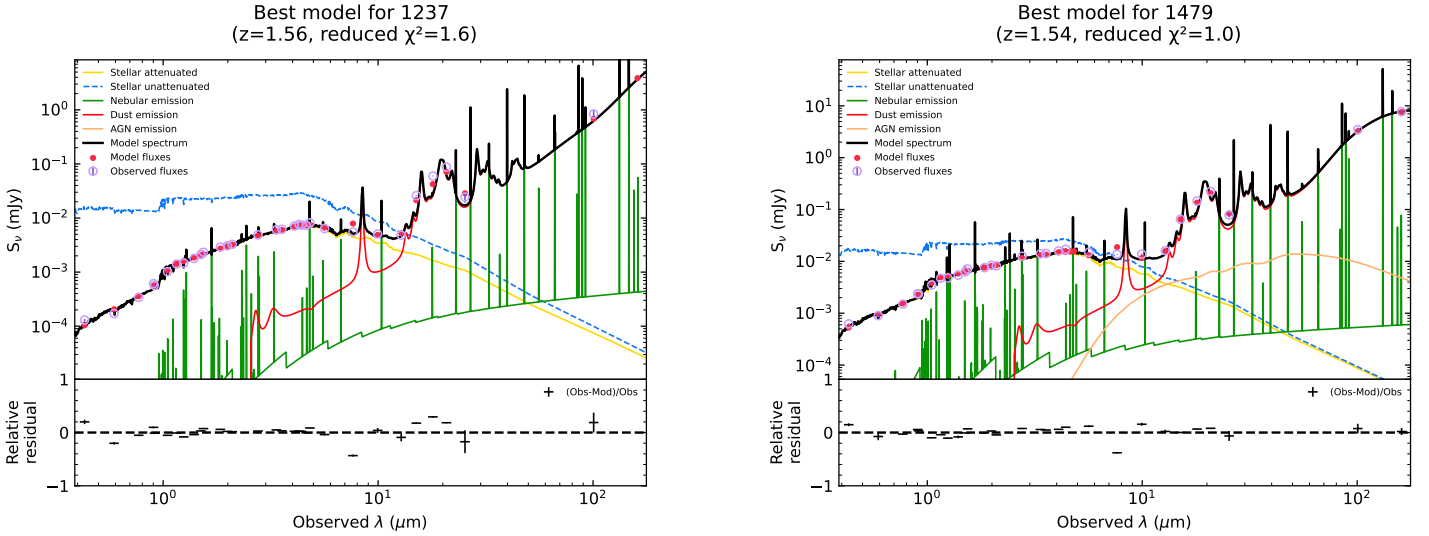


Fig. 5: Two examples (SMILES IDs 1237 and 1479) of the best-fitting SEDs of the MIRI-selected SFGs candidates at  $z \sim 1.5$ . The red and blue curves show the dust emission and the stellar emission, respectively. The purple circles show the observed photometric fluxes. The filled red circles are the model fluxes. The best model for 1479 requires an AGN component; in 1237 there is no AGN.

To quantify the success rate of our AGN selection based on a different validation metric, we compare with the MIRI-selected AGN sample of Lyu et al. (2024) in the SMILES survey. Their AGN selection includes various selection methods, including SED analysis and multi-wavelength properties such as X-ray detection, radio counterpart, and variability. They have 26 AGN

that satisfy the  $z$  conditions we apply. The legend of Fig. 4 reflects the red triangles of Lyu et al. (2024) AGN; 18 of these are overlapping with our AGN candidates. Our MIRI AGN limits have chosen 18 of their AGN. Based on this comparison, we estimate the success rate of our AGN selection to be at least 69 percent. Among the remaining eight AGN in Lyu et al. (2024)

sample, seven of them lie in the composite region of the bottom left and right panels in Fig. 4 (Kirkpatrick et al. 2017), and one lies in our SFGs region (top right panel in Fig. 4). However, for this case, the SFG region overlaps with the AGN region, and the same source is classified as AGN in the middle panel; so this discrepancy is related to the overlapping boundary region for these colors. Kirkpatrick et al. (2017) diagrams (bottom left and right panels in Fig. 4) are effective at isolating AGN via their red dust continuum. Lyu et al. (2024) AGN sample has been identified through the MIRI SED analysis, and some sources may appear near or within composite/SFGs region in Kirkpatrick et al. (2017) diagrams, since low-luminosity, obscured, or geometrically diluted AGN broadband photometry is dominated by host galaxy star formation. For lower luminosity AGN that can not produce a red, power-law-like MIR slope the SED analysis would still isolate the subdominant AGN component even when the integrated colors cannot separate the AGN. We also note that none of our Si absorption-dominated candidates are in their AGN sample.

As reported by Kirkpatrick et al. (2023), AGN regions in color diagrams can be contaminated by MIR weak galaxies, and this might also be possible for some of the candidates shown in Fig. 4. Since MIR weak galaxies do not indicate a specific MIR class, it is not possible to assign them to a class in this work. Some of the AGN that are not in the sample of Lyu et al. (2024) might be such MIR weak galaxies.

### 6.3. MIRI selected SFGs toward cosmic noon

We obtained the total IR luminosity ( $L_{IR}$ ), SFR, and stellar mass ( $M_{star}$ ) of 154 SFGs candidates from the SED analysis. The AGN contribution to  $L_{IR}$  ( $frac_{AGN}$ , in the 3-30 micron range) is zero for 84 sources,  $frac_{AGN} \leq 0.05$  for 74 sources and  $frac_{AGN} = 0.1$  for 13 sources. The low AGN contribution values ( $frac_{AGN} \leq 0.1$ ) confirm that these sources are SFGs. In addition, FIR radiation, which is a strong indicator of SF in galaxies, has been detected (in the GOODS-*Herschel* catalog Elbaz et al. 2011) for 29 sources. Hence, at least 19 percent of the SFGs candidates are secure SFGs.

Since AGN contribution is not zero for some sources, we compute  $L_{IR}$  as the sum of the dust luminosity and AGN luminosity. Most of the SFGs galaxies in our sample are normal SFGs with  $10^{8.0} L_{\odot} < L_{IR} < 10^{12.4} L_{\odot}$ . Among our SFGs candidates, there are 25 LIRGs<sup>2</sup> and three ULIRGs<sup>3</sup> at  $0.9 \leq z \leq 1.6$  (4 of which are starbursts with SFR > 100). And there are 20 LIRGs<sup>4</sup> and three ULIRGs<sup>5</sup> at  $z \sim 2$  (6 of which are starbursts with SFR > 100).

Lin et al. (2024) applied  $\log(F(15 \mu\text{m})/F(10 \mu\text{m})) > 0.8$  color selection determined from SED templates to identify PAH luminous SFGs at  $z \sim 1$  in the Cosmic Evolution Early Release Science (CEERS) MIRI survey. Our  $\log(F(15 \mu\text{m})/F(10 \mu\text{m})) > 1.0$  criteria agree well with theirs. Their sample includes ten SFGs with total IR luminosities of  $10^{10} \sim 10^{11.5} L_{\odot}$  at  $z \sim 1$ . They report their sample of normal SFGs to be on the star formation main sequence (MS, a tight correlation between SFR and stellar mass) at  $z \sim 1$ .

The location of our SFGs sample of 90 galaxies ( $0.9 \leq z \leq 1.6$ ) at  $z \sim 1$  MS is shown in (the left panel of) Fig. 6. For comparison, we show the  $z \sim 1$  SFGs sample of Lin et al. (2024) with gray diamonds. Our sample's  $M_{star}$  spans a wider range than theirs. The MS relations for  $z = 1.1 - 1.4$  (Pearson et al. 2018) and  $z = 0.8 - 1.1$  (Elbaz et al. 2007) are shown by the dashed lines in Fig. 6. Most of our  $z \sim 1$  sample is distributed around the MS relation of Elbaz et al. (2007). The locations of four (two LIRGs and two ULIRGs)  $z \sim 1$  galaxies<sup>6</sup> above the MS relationships are compatible with starburst galaxies (e.g., Daddi et al. 2010; Genzel et al. 2010). In the left panel of Fig. 6 34  $z \sim 2$  SFGs are shown. Since their positions are above the dashed lines, their distribution indicates an evolution compared to the  $z \sim 1$  MS. As reported by Lin et al. (2024), compared to previous IR space telescopes, JWST reveals less massive, lower IR luminosity SFGs at high- $z$ ; our MIRI selected SFGs sample supports this result with a larger number of galaxies.

### 6.4. MIRI selected silicate absorption-dominated galaxies toward cosmic noon

The present MIRI color selection in this work is a promising tool to identify Si absorption-dominated galaxies at higher redshifts, up to  $z \sim 1.6$ . One of the most important results we have is the selection of Si absorption-dominated galaxies (3A) at high redshift. Our knowledge of *Spitzer* detected 3A galaxies is limited to 32 galaxies at  $z < 0.67$  and three galaxies at  $z = 1.7 - 1.85$ . Varying levels of silicate absorption, including the deep levels occasionally seen in IR-luminous low- $z$  galaxies, have also been measured at higher redshifts ( $z \sim 1 - 2$ ) (e.g., Houck et al. 2005; Hatziminaoglou et al. 2015, and references therein). The selected 3A class candidates in this work might be the first JWST high- $z$  examples.

To investigate the nature of the MIRI-selected Si absorption galaxy candidates, we performed SED analysis using the modules listed in Table 1 with parameter settings used for the AGN candidates (described in section 6.2). The observed silicate absorption in 3A galaxies has been associated with differences in the distribution and geometry of the obscuring nuclear dust (Spoon et al. 2007). Spectroscopic studies of low- $z$  samples suggested that while modest silicate absorption can be produced in the clumpy medium of AGN torus, extremely deep silicate absorption can only be produced by a bright source buried in a smooth distribution of geometrically and optically thick dust within the host galaxy (Imanishi et al. 2007; Levenson et al. 2007; Goulding et al. 2012). The SEDs of the most deeply buried nuclei can be fitted with radiative transfer models for both the dust surrounding the nuclear source (e.g., the AGN torus) and the additional contributions from the host (e.g., González-Martín et al. 2019b; Efstathiou et al. 2022, and references therein). A broad and deep absorption feature specifically indicates that cold silicate dust with a high optical depth and dust coverage absorbs the bright infrared hot-dust continuum from the AGN at  $9.7 \mu\text{m}$  (e.g., Levenson et al. 2007; Stalevski et al. 2011; González-Martín et al. 2013, 2019b). Therefore, in our SED analysis with CIGALE, the most important component that allows us to decide whether these galaxies have silicate absorption features originating from obscured nuclei is the SKIRTOR AGN (Stalevski et al. 2012, 2016) that is widely used to model AGN MIR SEDs (e.g., González-Martín et al. 2019b). The SKIRTOR model assumes a high-density clumpy and low-density continuous and/or smooth toroidal dust distribution with a mixture of silicate and graphite

<sup>2</sup> SMILES ID:8, 55, 73, 339, 481, 486, 623, 1032, 1071, 1146, 1179, 1182, 1205, 1237, 1253, 1279, 1301, 1304, 1479, 1484, 1501, 1681, 1773, 1788, 1809

<sup>3</sup> SMILES ID:443,1373,1451

<sup>4</sup> SMILES ID:135, 222, 223, 261, 336, 343, 377, 378, 581, 709, 829, 864, 878, 1014, 1196, 1256, 1540, 1686, 1699, 1813

<sup>5</sup> SMILES ID:358,720,988

<sup>6</sup> SMILES ID:443,1182,1451,1479

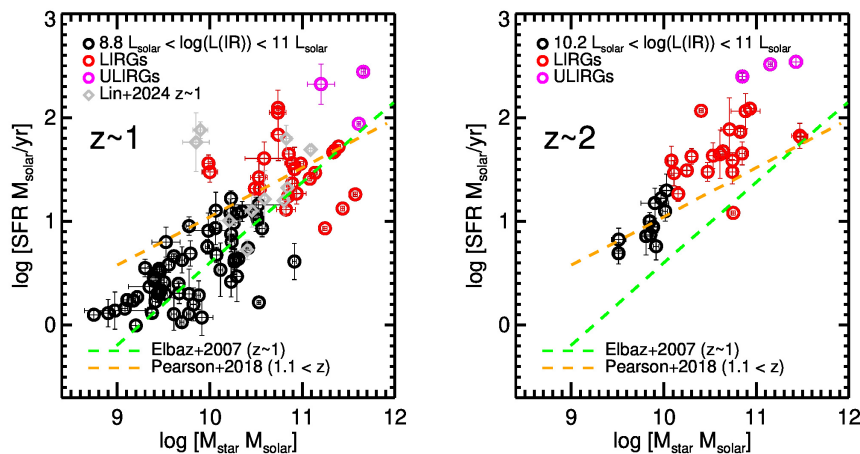


**Fig. 6.** Left panel: Distribution of our  $z \sim 1$  MIRI-selected SFGs over the SFR– $M_{\odot}$  correlation at  $z \sim 1$ . The SFR and  $M_{\text{star}}$  are obtained from the SED analysis. The green dashed line is  $z = 0.8 - 1.2$  MS relation of Elbaz et al. (2007). The orange dashed line is  $z = 1.1 - 1.4$  the MS relation from Pearson et al. (2018). The gray diamonds are the MIRI-selected SFGs sample of Lin et al. (2024). The majority of our  $z \sim 1$  sample is consistent with the MS relation of Elbaz et al. (2007). Right panel: Distribution of our MIRI-selected SFGs at  $z \sim 2$  over the SFR– $M_{\odot}$  correlation at  $z \sim 1$ . The distribution of the  $z \sim 2$  SFGs indicates an evolution compared to  $z \sim 1$  MS.

grains and a standard interstellar medium (ISM) dust composition. The main parameters of the SKIRTOR are the torus inclination ( $i$ , where  $i = 0^{\circ}$  represents a face-on type 1 AGN and  $i = 90^{\circ}$  an edge-on type 2 AGN), the torus average edge-on (equatorial) optical depth at  $9.7 \mu\text{m}$  ( $\tau_{\text{AGN}}$ ), the torus ratio of outer to inner radius ( $R = R_{\text{out}}/R_{\text{in}}$ ), and the torus half-opening angle ( $oa_{\text{AGN}}$ ). In this model, the shape of the silicate feature is a function of  $i$ ,  $\tau_{\text{AGN}}$ , dust distribution parameters, clump size, and arrangement (Stalevski et al. 2011). If the torus is viewed edge-on, the light from the AGN is absorbed more, resulting in a deeper feature. If viewed face-on, the feature might be shallower due to less dust along the line of sight. A high optical depth means a large fraction of the incident light at  $9.7 \mu\text{m}$  is being absorbed. For the  $R$  parameter the inner radius is assumed to be the dust sublimation radius, a smaller value means a compact torus and a larger value means an extended torus. The torus half-opening angle is a measure of the dust-filled region from the equator to the edge of the torus.

Based on the measured SED parameters, an edge-on view with  $i = 90^{\circ}$  and a high  $\tau_{\text{AGN}} = 11$  value identifies the candidate as a heavily obscured AGN with deep silicate absorption. Two galaxies, SMILES IDs 407 and 1052 have  $\tau_{\text{AGN}} = 11$ ,  $i = 90^{\circ}$  and  $frac_{\text{AGN}} = 0.4 - 0.5$ . Based on these parameters, we find it very likely that two (with SMILES IDs 407 and 1052) of the six candidates are Si absorption-dominated galaxies. The obtained best-fitting SEDs of two candidates are shown in Fig. 7 support an obscured AGN. As seen in these SEDs, the SKIRTOR AGN model with the largest possible  $\tau_{\text{AGN}}$  value of 11 is not extreme enough to produce the very deep silicate absorption feature for these galaxies, because the observed flux is even lower than the absorption feature of the model. González-Martín et al. (2019a) compared SED fitting results of six AGN torus models for a sample of 110 AGN with *Spitzer*/IRS spectroscopy and reported that the SKIRTOR model is among the other five AGN torus models that are not enough to describe the very deep silicate absorption feature. Efstathiou et al. (2022) present SED fitting comparison of different AGN torus models including the CYPRUS models for Galaxies and their Nuclear Spectra (CYGNUS) and report that most of the AGN torus models such as SKIRTOR do not produce deep enough silicate absorption features for their ULIRG sample. Identifying and eliminating the limits of current AGN torus models is beyond the scope of this work. Among the existing models, the SKIRTOR model is generally sufficient to provide a general understanding of the nature of the identified candidates, which is our goal. However, it is not possible to reach a definitive conclusion about the silicate strength of our candi-

dates without MIR spectroscopy. However, these galaxies have a very high probability of having a deeper silicate absorption feature than the deepest feature that can be obtained from the SKIRTOR model; therefore we interpret these sources as strong Si absorption-dominated galaxy candidates.

Here, we have demonstrated the power of MIRI colors to find Si absorption-dominated galaxies beyond the local Universe. García-Bernete et al. (2022) presents JWST MIRI color diagrams to select the most obscured galaxy nuclei in CONs based on CYGNUS SED model fitting results of local U/LIRGs selected from the IDEOS sample. Their color limits are model dependent while our color measurements are derived from observed MIR spectra. We also note that their sample was selected to be galaxies with high total IR luminosities. Since the deep Si absorption is also expected to be a prominent feature in the spectra of CONs in local U/LIRGs, our  $z = 1$   $\log(F(21 \mu\text{m})/F(15 \mu\text{m})) < -0.7$  color limit agrees well with their CONs limit of  $\log(F(21 \mu\text{m})/F(15 \mu\text{m})) < -1.0$  (García-Bernete et al. 2022). García-Bernete et al. (2025) present JWST color-color diagrams for selecting deeply obscured nuclei at higher redshifts, however we can not make a direct comparison because of the different color bands used. We note that these galaxies might also be CONs, that have supermassive black hole accretion and/or compact star-forming activity which is completely obscured by dust. MIRI spectroscopy is needed to apply CONs criteria (e.g., Donnan et al. 2023, and references therein) to find out if these are completely obscured nuclei.

As a result of the SED analysis, we found that the other three Si absorption-dominated galaxy candidates have no AGN contribution, their  $frac_{\text{AGN}} = 0.0$ . These galaxies might be dusty star-forming galaxies with a deep silicate absorption feature since the silicate absorption might also be produced by gas and dust in the host galaxy (e.g., Levenson et al. 2007; Goulding et al. 2012). These galaxies (SMILES IDs 1141, 1323, 2677) might contain buried nuclei of strong star-forming processes.

### 6.5. Comparison of MIRI color selection results with emission line ratio AGN and/or galaxy diagnostics

To compare our MIRI color selection with other AGN and galaxy classification methods based on emission line ratios we used the available  $[\text{O III}]\lambda 5007$ ,  $H\beta$ , emission line fluxes of 13 AGN (four at  $z = 0.28$  and nine at  $z = 0.62$ ) and ten SFGs (one at  $z = 0.28$  and nine at  $z = 0.62$ ) from MUSE Hubble Ultra Deep Field surveys DR 2 Main source catalog. We compared our AGN and SFG selection with that of Juneau et al. (2014). For  $z = 0.28$ , we

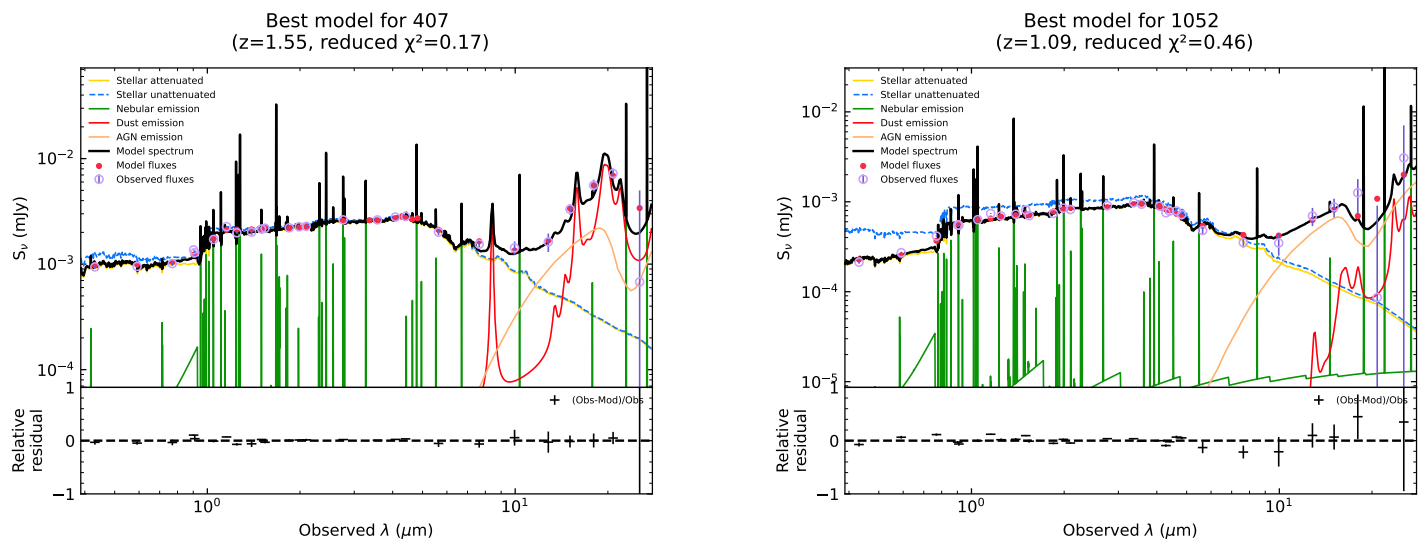


Fig. 7: Best-fitting SEDs of the MIRI-selected candidates likely to be Si absorption-dominated galaxies according to SED model parameters.

used their low-redshift criteria (their figure 1) and for  $z = 0.62$  we used their intermediate- $z$  criteria (their figure 4). All of our SFGs candidates are located in their SFGs region, so our SFG selection is consistent with their method. The agreement is not good for AGN, only 3/13 of our AGN are lying in their AGN region (both are 1A). However, they also report more discrepancies with IR-detected AGN; only 1/6 in the AGN region. Our ratio of IR-detected galaxies lying in the AGN region is close to theirs. As stated by Juneau et al. (2014), some IR AGN candidates may have contamination by SFGs; however, we note that our candidates' existing spectral data are insufficient to reach a full conclusion. Based on the limited number of spectra, this comparison shows a possibility of misclassifications at least for some of the AGN candidates.

Mazzolari et al. (2024) presented a new AGN selection technique based on  $[\text{O III}]\lambda 4363$  which is accessible with JWST. Unfortunately, none of our MIRI selected AGN and SFG candidates have NIRSpec measurements in JADES Data Release 3 (DR3) catalog. Therefore, we can not make a direct comparison with the  $[\text{O III}]\lambda 4363/H\gamma$  ratio classification (Mazzolari et al. 2024). To further expand its place in the broader context of AGN selection techniques, the MIR-based method presented here will be compared in detail with the optical-based methods (e.g., Juneau et al. 2014; Mazzolari et al. 2024) when optical spectra become available in the future.

### 6.6. Physical interpretation of MIR colors in the framework of galaxy evolution

MIR wavelengths ( $\sim 330 \mu\text{m}$ ) are sensitive to dust properties, star formation activity, AGN heating. Therefore, the MIR color classification of galaxies reveal evolutionary stages through distinct physical mechanisms: strong PAH emission indicates star formation, silicate absorption and dust geometry mark obscured transitional phases, and suppressed PAH features with elevated continuum signal AGN emergence Spoon et al. (e.g., 2006, 2022). In this work, we followed Spoon et al. (2022) and investigated new MIRI colors based on the relative strengths of Si absorption feature and PAH features that provide insights into the interstellar

medium (ISM) conditions and energy sources in galaxies. The six colors we show in Fig. 1 and Fig. 2, traces Si97 at different redshifts. In each panel the color in the y-axis traces the Si strength; the more negative colors means higher Si strength. Therefore, these colors reveal the obscuration levels at different types of galaxies, the most obscured galaxies clearly found closer to the bottom region. This is also relevant for the colors on the x-axis; they trace the Si strength in the opposite direction, toward the left: the more negative value means higher Si strength. Therefore, the obscuration level increases toward the left in these panels. In most panels AGN distribute around color values of 0 as expected; they exhibit stronger MIR continuum emission due to dust heated by the AGN activity and exhibit weaker/non PAH features. The MIR colors on the y-axis also trace the continuum-to-PAH ratio; lower values mean PAH emission is higher. In contrast, higher values toward the upper region mean low ratios as expected in AGN. Therefore, SFGs have lower values compared to AGN. In Fig. 1 we also investigated the colors of "transition" galaxies (classes 2A3B) with mixed MIR signatures, suggesting an evolutionary link between starburst-dominated and AGN-dominated systems. These galaxies may represent a phase where AGN feedback begins to quench star formation, marking a critical stage in galaxy evolution.

Spoon et al. (2022) demonstrated the use of MIR color-color diagrams to classify galaxies based on their dominant energy sources: star formation, AGN activity, or a mix of both. We extended their MIR color diagnostics to intermediate redshifts with recent JWST observations. Our MIRI color diagnostics that can distinguish between AGN (with hot dust continuum emission), SFGs (dominated by PAH features) and, Si absorption dominated galaxies are consistent with the diagnostics of Spoon et al. (2022). Galaxy-evolution scenarios (e.g., Hopkins et al. 2008a) suggest that when normal SFGs (e.g., 1C class) merge, they become "transition" galaxies (2A3B classes) going through strong nuclear obscuration before ending up as a naked AGN (class 1A). So our MIRI color diagrams at intermediate redshifts can be used to identify galaxies at different stages of galaxy evolution.

## 7. Conclusions

We obtained  $z$ -dependent ( $0.25 < z < 2.10$ ) *JWST*/MIRI color diagnostics based on *Spitzer* spectral features. We applied the MIR spectral classification diagnostics obtained in §2.2 to classify galaxies in the SMILES survey. We have made the classification code and the GMM region files publicly available.<sup>7</sup> Our conclusions are summarized below.

1. We show that combinations of MIRI colors alone can identify different MIR classes when the redshift is known.
2. Our MIRI color limits provide an effective tool to separate samples of SFGs (1C & 2C), AGN (1A & 1B), and Si absorption-dominated galaxies (3A) at cosmic noon.
3. Compared to previously known 3A galaxies observed with *Spitzer*, our 3A candidates are the first *JWST* high-redshift examples to date.
4. The MIRI-selected SFGs identified in this work show that *JWST* finds a diversity of high- $z$  SFGs, including those with lower masses and IR luminosities.
5. The majority of MIRI-selected SFGs at  $0.9 < z < 1.6$  identified in this work, are consistent with the  $z \sim 1$  MS. Our MIRI-selected SFGs at  $z \sim 2$  indicate an evolution compared to  $z \sim 1$  MS.

We used MIRI's unique continuous MIR filter coverage and obtained improved color diagnostics for MIR galaxy classification. As a future prospect, we will apply the  $z$ -dependent *JWST*/MIRI color diagnostics introduced in this work to other completed and future *JWST*/MIRI survey data. We also aim to improve our method with NIRspec emission line measurements to be obtained in the future. Increasing the number of MIRI classified SFGs, AGN, and Si absorption-dominated galaxies toward cosmic noon will contribute to our understanding of galaxy evolution by revealing the characteristics of larger samples.

*Acknowledgements.* We thank the anonymous referee for carefully reading the manuscript and for suggestions and recommendations, which have substantially improved the quality and clarity of the paper. TG acknowledges the support of the National Science and Technology Council of Taiwan through grants 113-2112-M-007-006, TH acknowledges the support of the National Science and Technology Council of Taiwan through grants 110-2112-M-005-013-MY3, 110-2112-M-007-034-, 113-2123-M-001-008-, and 113-2112-M-005-009-MY3. This work is based on observations made with the NASA/ESA/CSA James Webb Space Telescope. The data were obtained from the Mikulski Archive for Space Telescopes at the Space Telescope Science Institute, which is operated by the Association of Universities for Research in Astronomy, Inc., under NASA contract NAS 5-03127 for *JWST*. These observations are associated with the program ERO. The authors acknowledge the CEERS team for developing their observing program with a zero-exclusive-access period. This work is based on observations taken by the CANDELS Multi-Cycle Treasury Program with the NASA/ESA *HST*, which is operated by the Association of Universities for Research in Astronomy, Inc., under NASA contract NAS 5-26555. Some of the data presented in this paper were obtained from the Mikulski Archive for Space Telescopes (MAST) at the Space Telescope Science Institute. The specific observations analyzed can be accessed via doi:10.17909/agda-2w34.

## References

Alberts, S., Lyu, J., Shivaee, I., et al. 2024, *ApJ*, 976, 224  
 Armus, L., Charmandaris, V., Spoon, H. W. W., et al. 2004, *ApJS*, 154, 178  
 Assef, R. J., Stern, D., Kochanek, C. S., et al. 2013, *ApJ*, 772, 26  
 Bacon, R., Brinchmann, J., Conseil, S., et al. 2023, *A&A*, 670, A4  
 Beckwith, S. V. W., Stiavelli, M., Koekemoer, A. M., et al. 2006, *AJ*, 132, 1729  
 Boquien, M. et al. 2019, *A&A*, 622, A103  
 Bornancini, C. & García Lambas, D. 2020, *MNRAS*, 494, 1189  
 Brammer, G. B., van Dokkum, P. G., & Coppi, P. 2008, *ApJ*, 686, 1503  
 Bruzual, G. & Charlot, S. 2003, *MNRAS*, 344, 1000

Calzetti, D., Armus, L., Bohlin, R. C., et al. 2000, *ApJ*, 533, 682  
 Calzetti, D., Kennicutt, R. C., Engelbracht, C. W., et al. 2007, *ApJ*, 666, 870  
 Charlot, S. & Fall, S. M. 2000, *ApJ*, 539, 718  
 da Cunha, E., Charlot, S., & Elbaz, D. 2008, *MNRAS*, 388, 1595  
 Daddi, E., Elbaz, D., Walter, F., et al. 2010, *ApJ*, 714, L118  
 D'Eugenio, F., Cameron, A. J., Scholtz, J., et al. 2024, arXiv e-prints, arXiv:2404.06531  
 Donnan, F. R., Rigopoulou, D., García-Bernetete, I., et al. 2023, *A&A*, 669, A87  
 Draine, B. T. et al. 2014, *ApJ*, 780, 172  
 Efstathiou, A., Farrah, D., Afonso, J., et al. 2022, *MNRAS*, 512, 5183  
 Efstathiou, A. & Rowan-Robinson, M. 2003, *MNRAS*, 343, 322  
 Eisenstein, D. J., Willott, C., Alberts, S., et al. 2023, arXiv e-prints, arXiv:2306.02465  
 Elbaz, D., Daddi, E., Le Borgne, D., et al. 2007, *A&A*, 468, 33  
 Elbaz, D., Dickinson, M., Hwang, H. S., et al. 2011, *A&A*, 533, A119  
 Farrah, D., Bernard-Salas, J., Spoon, H. W. W., et al. 2007, *ApJ*, 667, 149  
 García-Bernetete, I., Donnan, F. R., Rigopoulou, D., et al. 2025, arXiv e-prints, arXiv:2502.16301  
 García-Bernetete, I., Rigopoulou, D., Aalto, S., et al. 2022, *A&A*, 663, A46  
 Genzel, R., Tacconi, L. J., Gracia-Carpio, J., et al. 2010, *MNRAS*, 407, 2091  
 González-Martín, O., Masegosa, J., García-Bernetete, I., et al. 2019a, *ApJ*, 884, 11  
 González-Martín, O., Masegosa, J., García-Bernetete, I., et al. 2019b, *ApJ*, 884, 10  
 González-Martín, O., Rodríguez-Espinosa, J. M., Díaz-Santos, T., et al. 2013, *A&A*, 553, A35  
 Goulding, A. D., Alexander, D. M., Bauer, F. E., et al. 2012, *ApJ*, 755, 5  
 Grogin, N. A., Kocevski, D. D., Faber, S. M., et al. 2011, *ApJS*, 197, 35  
 Hatziminaoglou, E., Hernán-Caballero, A., Feltre, A., & Piñol Ferrer, N. 2015, *ApJ*, 803, 110  
 Hernán-Caballero, A., Spoon, H. W. W., Lebouteiller, V., Rupke, D. S. N., & Barry, D. P. 2016, *MNRAS*, 455, 1796  
 Hopkins, P. F., Cox, T. J., Kereš, D., & Hernquist, L. 2008a, *ApJS*, 175, 390  
 Hopkins, P. F., Hernquist, L., Cox, T. J., & Kereš, D. 2008b, *ApJS*, 175, 356  
 Houck, J. R., Roellig, T. L., Van Cleve, J., et al. 2004, in *Society of Photo-Optical Instrumentation Engineers (SPIE) Conference Series*, Vol. 5487, *Optical, Infrared, and Millimeter Space Telescopes*, ed. J. C. Mather, 62–76  
 Houck, J. R., Soifer, B. T., Weedman, D., et al. 2005, *ApJ*, 622, L105  
 Ichikawa, K., Ricci, C., Ueda, Y., et al. 2019, *ApJ*, 870, 31  
 Imanishi, M., Dudley, C. C., Maiolino, R., et al. 2007, *ApJS*, 171, 72  
 Juneau, S., Bournaud, F., Charlot, S., et al. 2014, *ApJ*, 788, 88  
 Kessler, M. F., Steinz, J. A., Anderegg, M. E., et al. 1996, *A&A*, 315, L27  
 Kirkpatrick, A., Alberts, S., Pope, A., et al. 2017, *ApJ*, 849, 111  
 Kirkpatrick, A., Pope, A., Charmandaris, V., et al. 2013, *ApJ*, 763, 123  
 Kirkpatrick, A., Yang, G., Le Bail, A., et al. 2023, arXiv e-prints, arXiv:2308.09750  
 Kodra, D., Andrews, B. H., Newman, J. A., et al. 2023, *ApJ*, 942, 36  
 Leitherer, C., Li, I. H., Calzetti, D., & Heckman, T. M. 2002, *ApJS*, 140, 303  
 Levenson, N. A., Sirocky, M. M., Hao, L., et al. 2007, *ApJ*, 654, L45  
 Lin, Y.-W., Wu, C. K. W., Ling, C.-T., et al. 2024, *MNRAS*, 527, 11882  
 Ling, C.-T., Kim, S. J., Wu, C. K. W., et al. 2022, *MNRAS*, 517, 853  
 Lyu, J., Alberts, S., Rieke, G. H., et al. 2024, *ApJ*, 966, 229  
 Maas, R., Hyrkas, J., Telford, O. G., et al. 2015, in *Proceedings of the 3rd VLDB Workshop on In-Memory Data Management and Analytics, IMDM '15* (New York, NY, USA: Association for Computing Machinery)  
 Magnelli, B., Popesso, P., Berta, S., et al. 2013, *A&A*, 553, A132  
 Mateos, S., Alonso-Herrero, A., Carrera, F. J., et al. 2013, *MNRAS*, 434, 941  
 Mazzolari, G., Übler, H., Maiolino, R., et al. 2024, *A&A*, 691, A345  
 Noll, S., Burgarella, D., Giovannoli, E., et al. 2009, *A&A*, 507, 1793  
 Oesch, P. A., Brammer, G., Naidu, R. P., et al. 2023, *MNRAS*, 525, 2864  
 Pearson, W. J., Wang, L., Hurley, P. D., et al. 2018, *A&A*, 615, A146  
 Pedregosa, F., Varoquaux, G., Gramfort, A., et al. 2011, *Journal of Machine Learning Research*, 12, 2825  
 Peeters, E., Spoon, H. W. W., & Tielens, A. G. G. M. 2004, *ApJ*, 613, 986  
 Rieke, G. H., Alberts, S., Shivaee, I., et al. 2024, *ApJ*, 975, 83  
 Rieke, G. H., Wright, G. S., Böker, T., et al. 2015, *PASP*, 127, 584  
 Rieke, M. J., Robertson, B., Tacchella, S., et al. 2023, *ApJS*, 269, 16  
 Rovilos, E., Georgantopoulos, I., Akylas, A., et al. 2014, *MNRAS*, 438, 494  
 Salpeter, E. E. 1955, *ApJ*, 121, 161  
 Sanders, D. B., Soifer, B. T., Elias, J. H., et al. 1988, *ApJ*, 325, 74  
 Serra, P. et al. 2011, *ApJ*, 740, 22  
 Spergel, D. N. et al. 2003, *ApJS*, 148, 175  
 Spoon, H. W. W., Hernán-Caballero, A., Rupke, D., et al. 2022, *ApJS*, 259, 37  
 Spoon, H. W. W., Keane, J. V., Tielens, A. G. G. M., Lutz, D., & Moorwood, A. F. M. 2001, *A&A*, 365, L353  
 Spoon, H. W. W., Marshall, J. A., Houck, J. R., et al. 2007, *ApJ*, 654, L49  
 Spoon, H. W. W., Tielens, A. G. G. M., Armus, L., et al. 2006, *ApJ*, 638, 759  
 Stalevski, M., Fritz, J., Baes, M., Nakos, T., & Popović, L. C. 2011, *Open Astronomy*, 20, 490  
 Stalevski, M., Fritz, J., Baes, M., Nakos, T., & Popović, L. C. 2012, *MNRAS*, 420, 2756  
 Stalevski, M., Ricci, C., Ueda, Y., et al. 2016, *MNRAS*, 458, 2888  
 Stern, D., Assef, R. J., Benford, D. J., et al. 2012, *ApJ*, 753, 30  
 Veilleux, S., Kim, D. C., & Sanders, D. B. 2002, *ApJS*, 143, 315  
 Werner, M. W., Roellig, T. L., Low, F. J., et al. 2004, *ApJS*, 154, 1  
 Williams, C. C., Tacchella, S., Masada, M. V., et al. 2023, *ApJS*, 268, 64  
 Wright, G. S., Rieke, G. H., Glasse, A., et al. 2023, *Publications of the Astronomical Society of the Pacific*, 135, 048003  
 Wu, C. K. W., Ling, C.-T., Goto, T., et al. 2023, *MNRAS*, 523, 5187  
 Yang, G., Caputi, K. I., Papovich, C., et al. 2023a, *ApJ*, 950, L5  
 Yang, G., Papovich, C., Bagley, M., et al. 2023b, arXiv e-prints, arXiv:2307.14509  
 Yang, G. et al. 2022, *ApJ*, 927, 192

<sup>7</sup> <https://github.com/Ecekilerci/MIRIcolordiagnositics>

## Appendix A: PAH equivalent width correlations

As shown in Fig. A.1 PAH62 EQW positively correlates with PAH77 EQW (left panel), PAH112 EQW (middle panel), and PAH127 EQW (right panel). The strength of the correlations is given by Spearman's rank correlation coefficient ( $r_s$ ) in each panel. The  $r_s \geq 0.7$  values indicate a strong correlation between the EQW measurements. A significance value of 0.00 is found for each panel. Therefore, there is less than a 0.1% chance that the found  $r_s$  happened by chance if there were no correlations between these EQW measurements.

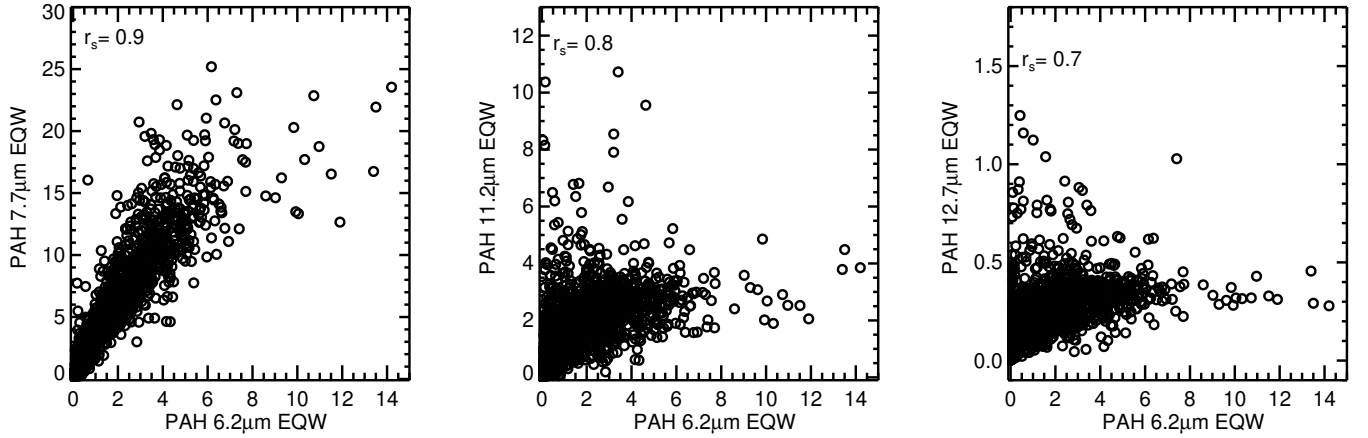


Fig. A.1: Correlations between PAH62 EQW and PAH77 EQW (left panel), PAH62 EQW and PAH112 EQW (middle panel), PAH62 EQW and PAH127 EQW (right panel). The Spearman's rank correlation coefficient  $r_s$  is listed in each panel. The significance of  $r_s$  is 0.00 for each panel.

## Appendix B: Gaussian mixture model regions

The color–color diagrams in Fig. 1 and Fig. 2 trace Si97 and one of the PAH62, PAH77, PAH112, PAH127 emission features for the given redshift range. GMM model regions of each MIR class in MIRI color–color diagrams shown in Fig. 1 are listed in Table B.1. GMM model regions of AGN (1A & 1B & 2A) and SFGs (1C & 2C) shown in Fig. 2 are given in Table B.2.

GMM model regions of AGN (1A & 1B & 2A) and SFGs (1C & 2C) on the color–color diagrams adopted from Kirkpatrick et al. (2017) and Kirkpatrick et al. (2023) are listed in Table B.3.

Table B.1: MIRI color regions of the distinct regions for 1A, 1B, 1C, 2A, 2B, 2C, 3A, 3B MIR spectral classes obtained by GMM analysis.

MIR Spectral Class	GMM Component Number	Center-x	Center-y	Width	Height	Angle
$z = 0.25 - 0.30$		$x = \log(F(12\ \mu\text{m})/F(07\ \mu\text{m}))$	$y = \log(F(12\ \mu\text{m})/F(10\ \mu\text{m}))$			
1A	1	0.2136	0.1010	0.7725	0.2554	-151.76
1B	1	0.1405	-0.2714	0.7421	0.2193	51.14
1B	2	0.2956	0.0346	0.8799	0.2484	-148.81
1C	1	0.0668	-0.4617	0.6951	0.1042	46.42
2A	1	-0.1108	-0.3437	1.1263	0.2648	-137.45
2B	1	-0.1437	-0.5728	0.9194	0.2671	45.63
2C	1	-0.1486	-0.6766	0.6242	0.0814	46.96
3A	1	-1.0145	-1.3882	1.1161	0.1251	-159.60
3A	2	-0.6624	-1.0225	0.8311	0.4586	-148.22
3B	1	-0.5175	-0.9988	0.6665	0.2075	46.41
$z = 0.58 - 0.65$		$x = \log(F(15\ \mu\text{m})/F(10\ \mu\text{m}))$	$y = \log(F(15\ \mu\text{m})/F(12\ \mu\text{m}))$			
1A	1	0.2223	0.0901	0.4058	0.1626	-152.83
1A	2	-0.0362	-0.0349	0.4776	0.2875	168.31
1B	1	0.0572	-0.2706	0.5917	0.1821	48.39
1B	2	0.2198	-0.0126	0.7063	0.2175	-151.94
1C	1	-0.0171	-0.4208	0.5500	0.0925	-136.46
2A	1	-0.1363	-0.2969	0.8477	0.2094	-138.03
2B	1	-0.1623	-0.4960	0.7192	0.2250	-136.37
2C	1	-0.1790	-0.5753	0.4598	0.0780	-135.77
3A	1	-0.5546	-0.8427	0.6569	0.4289	54.90
3A	2	-0.9630	-1.0037	0.7690	0.1308	-135.06
3B	1	-0.4387	-0.8116	0.5855	0.1887	-142.92
$z = 0.58 - 0.65$		$x = \log(F(15\ \mu\text{m})/F(10\ \mu\text{m}))$	$y = \log(F(15\ \mu\text{m})/F(21\ \mu\text{m}))$			
1A	1	0.1645	-0.1706	0.7842	0.4558	125.10
1B	1	0.1316	-0.3287	0.6184	0.5290	174.19
1C	1	-0.0175	-0.3730	0.4089	0.3226	-163.88
2A	1	-0.2511	-0.6972	0.5584	0.4719	160.99
2A	2	-0.0446	-0.5329	0.4604	0.4141	148.56
2A	3	0.0216	0.4006	0.0040	0.0040	90.00
2B	1	-0.1595	-0.6949	0.5957	0.4359	-137.49
2C	1	-0.1790	-0.6005	0.3497	0.2768	-150.99
3A	1	-0.5385	-1.1491	0.6612	0.4583	62.40
3A	2	-0.8235	-0.8866	0.8627	0.3868	-158.73
3B	1	-0.4387	-1.0327	0.5965	0.4613	69.04
$z = 0.90 - 0.92$		$x = \log(F(18\ \mu\text{m})/F(15\ \mu\text{m}))$	$y = \log(F(18\ \mu\text{m})/F(25\ \mu\text{m}))$			
1A	1	0.0620	-0.1843	0.7919	0.3452	84.79
1B	1	-0.1690	-0.3658	0.7754	0.5570	-146.37
1C	1	-0.4600	-0.4370	0.4368	0.3290	-152.04
2A	1	-0.4343	-0.7607	0.6632	0.3858	-151.14
2A	2	-0.2362	-0.5559	0.4416	0.3182	80.96
2A	3	-0.2645	0.7378	0.0040	0.0040	90.00
2B	1	-0.4399	-0.6913	0.4711	0.4005	-166.93
2B	2	-0.6278	-0.8295	0.5723	0.3141	62.65
2C	1	-0.6311	-0.6842	0.3964	0.2746	-147.89
3A	1	-1.0050	-1.2608	0.9251	0.0385	78.03
3A	2	-0.9489	-1.1386	0.9224	0.6395	-150.03
3B	1	-0.8938	-1.1434	0.6249	0.3745	64.89
$z = 1.0 - 1.10$		$x = \log(F(21\ \mu\text{m})/F(12\ \mu\text{m}))$	$y = \log(F(21\ \mu\text{m})/F(15\ \mu\text{m}))$			
1A	1	0.2755	0.1876	0.5124	0.1308	-143.85
1A	2	-0.0183	-0.0180	0.5535	0.2056	-164.56

Table B.1: continued.

MIR spectral class	GMM component number	Center-x	Center-y	Width	Height	Angle
1B	1	0.1921	-0.0708	0.6050	0.1593	49.85
1B	2	0.3074	0.1401	0.8460	0.1588	-145.31
1C	1	0.1106	-0.2261	0.3317	0.0751	-135.35
1C	2	0.1787	-0.1548	0.8551	0.0917	46.77
2A	1	-0.0363	-0.1863	0.3457	0.1764	49.30
2A	2	-0.3299	-0.4754	0.5355	0.2070	51.26
2A	3	0.1293	-0.0443	0.4671	0.0651	-136.98
2B	1	0.0105	-0.2834	0.6071	0.1680	48.29
2B	2	-0.1679	-0.4804	0.6337	0.1437	-145.14
2C	1	-0.0439	-0.3904	0.4944	0.0639	47.38
3A	1	-0.4238	-0.7611	0.4917	0.3458	-144.12
3A	2	-0.8580	-1.0474	0.7736	0.2880	46.86
3B	1	-0.3500	-0.7115	0.6622	0.1509	-137.49
<hr/>						
$z = 1.5 - 1.6$	$x = \log(F(25 \mu\text{m})/F(15 \mu\text{m}))$	$y = \log(F(25 \mu\text{m})/F(21 \mu\text{m}))$				
1A	1	0.2665	0.1009	0.5124	0.2261	-155.38
1A	2	-0.1073	-0.0384	0.4313	0.2235	140.32
1B	1	0.1664	-0.2492	0.6474	0.2368	49.84
1B	2	0.2948	0.0175	0.8338	0.2421	-155.00
1C	1	0.0879	-0.4460	0.4210	0.0955	-135.77
1C	2	0.2267	-0.2888	0.9494	0.1558	-137.10
2A	1	-0.0523	-0.2636	0.3369	0.2654	-144.10
2A	2	-0.3449	-0.5321	0.6425	0.3545	45.07
2A	3	0.1171	-0.1797	0.5414	0.1435	-136.15
2B	1	-0.0024	-0.4005	0.6143	0.2960	-140.51
2B	2	-0.1811	-0.6134	0.6439	0.2318	-148.39
2C	1	-0.0935	-0.6097	0.5508	0.0831	45.24
3A	1	-0.8536	-1.1305	1.0549	0.4287	-150.87
3A	2	-0.5237	-0.8977	0.6504	0.4879	-143.91
3B	1	-0.4423	-0.9013	0.5981	0.2219	-136.61

Table B.2: MIRI color regions of AGN (1A &amp; 1B &amp; 2A) and SFGs (1C &amp; 2C) obtained by GMM analysis.

MIR Spectral Class	GMM Component Number	Center-x	Center-y	Width	Height	Angle
<hr/>						
$z = 0.25 - 0.30$	$x = \log(F(12 \mu\text{m})/F(07 \mu\text{m}))$	$y = \log(F(12 \mu\text{m})/F(10 \mu\text{m}))$				
AGN	1	0.0636	-0.1598	0.8716	0.5999	46.50
AGN	2	0.2799	0.1273	0.5936	0.2344	-151.67
SFG	1	0.0284	-0.5036	0.6164	0.0925	45.43
SFG	2	0.1130	-0.3914	1.4444	0.1360	45.93
<hr/>						
$z = 0.58 - 0.65$	$x = \log(F(15 \mu\text{m})/F(10 \mu\text{m}))$	$y = \log(F(15 \mu\text{m})/F(12 \mu\text{m}))$				
AGN	1	-0.1287	0.0098	0.1682	0.0899	-165.61
AGN	2	0.2039	0.0867	0.3139	0.1347	-151.38
AGN	3	0.1298	-0.1029	0.9882	0.3110	-135.05
SFG	1	-0.0510	-0.4543	0.4295	0.0828	-137.31
SFG	2	0.0187	-0.3816	1.0395	0.1168	-136.05
<hr/>						
$z = 0.58 - 0.65$	$x = \log(F(15 \mu\text{m})/F(10 \mu\text{m}))$	$y = \log(F(15 \mu\text{m})/F(21 \mu\text{m}))$				
AGN	1	0.1638	-0.1813	0.7936	0.4391	127.87
AGN	2	0.1474	-99.0000	0.5178	0.0040	0.00
AGN	3	0.0774	-0.3832	0.8953	0.4909	46.58
SFG	1	-0.0381	-0.4021	0.5320	0.3431	-135.69
<hr/>						
$z = 0.90 - 0.92$	$x = \log(F(18 \mu\text{m})/F(15 \mu\text{m}))$	$y = \log(F(18 \mu\text{m})/F(25 \mu\text{m}))$				
AGN	1	0.0711	-0.1735	0.7970	0.2963	91.06
AGN	2	-0.2021	-0.4180	0.8312	0.5029	-137.04
SFG	1	-0.4818	-0.4686	0.5795	0.3402	46.54
<hr/>						
$z = 1.0 - 1.10$	$x = \log(F(21 \mu\text{m})/F(12 \mu\text{m}))$	$y = \log(F(21 \mu\text{m})/F(15 \mu\text{m}))$				
AGN	1	0.2195	0.0292	1.0563	0.2441	45.31
AGN	2	0.2509	0.1749	0.4313	0.1061	-142.75
AGN	3	-0.1217	-0.0240	0.2242	0.0531	-148.39
SFG	1	0.1263	-0.2096	0.5726	0.0836	46.01

Table B.2: continued.

MIR spectral class	GMM component number	Center-x	Center-y	Width	Height	Angle
SFG	2	0.0100	-0.3338	0.5926	0.0429	47.60
$z = 1.5 - 1.6$	$x = \log(F(25 \mu\text{m})/F(15 \mu\text{m}))$	$y = \log(F(25 \mu\text{m})/F(21 \mu\text{m}))$				
AGN	1	0.0318	0.0068	0.7793	0.1318	-177.57
AGN	2	0.2612	0.1185	0.3348	0.1401	-160.24
AGN	3	0.2078	-0.1020	1.1188	0.3863	-136.29
SFG	1	0.0736	-0.4591	0.5359	0.0920	-136.42
SFG	2	0.1315	-0.3798	1.2232	0.1519	-135.83

Table B.3: MIRI color regions of AGN (1A &amp; 1B &amp; 2A) and SFGs (1C &amp; 2C) on the color diagrams adopted from the literature obtained by GMM analysis.

MIR Spectral Class	GMM Component Number	Center-x	Center-y	Width	Height	Angle
$z = 1.0 - 1.1$	$x = \log(F(15 \mu\text{m})/F(07 \mu\text{m}))$	$y = \log(F(18 \mu\text{m})/F(10 \mu\text{m}))$				
AGN	1	0.3160	0.2809	1.5998	0.5815	-166.66
SFG	1	0.1559	0.6351	1.9786	0.8027	-158.90
$z = 1.4 - 1.5$	$x = \log(F(12 \mu\text{m})/F(10 \mu\text{m}))$	$y = \log(F(18 \mu\text{m})/F(10 \mu\text{m}))$				
AGN	1	0.1279	0.3031	0.6796	0.0968	65.77
AGN	2	0.1363	0.4754	3.2915	0.6395	47.97
SFG	1	-0.6842	0.0817	1.7547	0.4047	56.38
SFG	2	-0.3076	0.6029	3.4785	0.2054	-135.91
$z = 2.0 - 2.1$	$x = \log(F(18 \mu\text{m})/F(10 \mu\text{m}))$	$y = \log(F(21 \mu\text{m})/F(15 \mu\text{m}))$				
AGN	1	0.1827	0.1853	2.0844	0.6643	-176.12
SFG	1	-0.4165	0.7037	2.0901	0.8823	-164.58